Resonant three-dimensional nonlinear sloshing in a square base basin. Part 4. Oblique forcing and linear viscous damping

Odd M. Faltinsen[1]† and Alexander N. Timokha[1,2]

[1]Centre for Autonomous Marine Operations and Systems & Department of Marine Technology, Norwegian University of Science and Technology, NO-7491 Trondheim, Norway

[2]Institute of Mathematics, National Academy of Sciences of Ukraine, 01601 Kiev, Ukraine

(Received xx; revised xx; accepted xx)

Faltinsen *et al.* (2003) (henceforth, Part 1) examined an *undamped* nonlinear resonant steady-state sloshing in a square base tank by developing an approximate (asymptotic) Narimanov-Moiseev–type multimodal theory. A focus was on *longitudinal* and *diagonal* harmonic tank excitations. Neglecting the linear viscous boundary-layer damping was justified for model tanks with breadth in the order of meters. However, nonlinear sloshing in clean tanks of smaller size (count in centimetres) may be affected by damping in finite depth conditions. Qualitative and quantitative properties of the *damped* resonant steady-state sloshing in a square base tank are now studied by using the modal theory from Part 1 equipped with the linear damping terms. The tank harmonically oscillates along an arbitrary horizontal (*oblique*) direction. An analytical asymptotic steady-state *undamped solution* is derived and the corresponding response curves are analysed versus the forcing direction. When the tank width = breadth = $L \sim 10$ cm, the surface tension effect on the free surface dynamics can be neglected but the linear viscous damping should be included into the Narimanov-Moiseev nonlinear asymptotic modal theory. We *analytically* show that the steady-state *damped* sloshing possesses a series of distinguishing features so that, e.g., the squares-like standing wave regime fully disappears and becomes replaced by swirling. Typical response curves of the damped steady-state resonant sloshing are studied for the liquid depth-to-width ratio exceeding 0.5. The computational results of the steady-state resonant response amplitudes are in a satisfactory agreement with observations and measurements by Ikeda *et al.* (2012), which were conducted with a relatively small laboratory container.

1. Introduction

Part 1 (Faltinsen *et al.* 2003) initiated *theoretical and experimental* studies on the nonlinear resonant liquid sloshing in a square base tank performing either longitudinal (along a pair of parallel vertical walls) or diagonal harmonic excitation with the forcing frequency close to the lowest natural sloshing frequency. The theoretical *assumptions* were (a) an ideal incompressible liquid with irrotational flows, i.e. the damping can be neglected; (b) the mean liquid depth to the tank breadth L (= width) ratio is finite, (c) the surface tension effect on the free surface dynamic can be neglected, and (d) the forcing amplitude is small relative to the tank breadth. The latter nondimensional forcing amplitude η was associated with a small input parameter $\eta \ll 1$. The assumptions (a)–

† Email address for correspondence: odd.faltinsen@ntnu.no

(d) *are relevant* for many clean (without internal structures, e.g., baffles, screens or bulkheads) rectangular industrial tanks.

By adopting the Narimanov-Moiseev (Duffing–type) asymptotic technique, Part 1 derived a nonlinear approximate (asymptotic) multimodal system governing the generalised coordinates of the nine natural sloshing modes, which are characterised by the orders $O(\eta^{1/3}), O(\eta^{2/3})$ and $O(\eta)$. An asymptotic *steady-state (periodic) solution* of the multimodal system was derived to quantify the frequency ranges where the stable and unstable steady-state resonance wave regimes occur. This steady-state analysis (called the *classification*) was supported by model tests (Faltinsen *et al.* 2003, 2005*a*) conducted in a rigid tank with a cross-section of 1×1 m. Faltinsen *et al.* (2005*b*) (Part 2) showed that increasing the forcing amplitude (the input parameter η) requires an adaptive (not Narimanov-Moiseev's one) asymptotic ordering. Using the corresponding adaptive modal systems is also needed for smaller liquid depths and to better describe transient waves. The adaptive ordering accounts for the secondary resonances in the hydrodynamic system. Faltinsen *et al.* (2006*a*) (Part 3) investigated the aspect ratio effect of the square base.

These studies on resonant sloshing in a square base tank were followed up by many authors who conducted numerical simulations (Wu & Chen 2009; Wu *et al.* 2013*b*,*a*), made new model tests (Ikeda *et al.* 2012) and/or derived their own versions of the (adaptive) multimodal theory (Ikeda *et al.* 2012; Pilipchuk 2013; Zhang *et al.* 2014; Ikeda *et al.* 2016). In major cases, assumptions (a)–(d) were common and, therefore, the results were in agreement with Parts 1–3. In particular, they *confirmed* the established stability ranges for (i) the standing resonant wave occurring in the excitation plane (planar and diagonal for longitudinal and diagonal forcing, respectively), (ii) the squares-like sloshing (the standing waves by a combined Stokes mode occurring at an angle to the excitation plane), (iii) the two physically-identical (angularly propagating clockwise and counterclockwise) swirling waves, whose wave elevations at the perpendicular walls were equal for the diagonal forcing, and (iv) the irregular (chaotic) waves in the frequency ranges where (i)–(iii) are unstable. Against this background, experimental observations and measurements of the steady-state resonant sloshing in a horizontally-shaken square base tank by Ikeda *et al.* (2012) look rather contradictory.

Ikeda *et al.* (2012) investigated the resonant steady-state sloshing for an arbitrary (including oblique) harmonic horizontal forcing and reported that (i') the purely standing resonant waves in the excitation plane exist *exclusively* for the longitudinal and diagonal excitations (never for an oblique one), (ii') the purely squares-like standing waves (see, definition in (ii)) do not exist anymore, they are replaced by swirling or, alternatively, by an almost standing wave, which is formally swirling where one from two modified Stokes modes dominates, (iii') except for the longitudinal forcing, the two physically-identical swirling modes of different propagating directions split into two different swirling wave regimes so that, e.g., the maximum wave elevations at the two perpendicular walls become non-equal for the diagonal forcing. The differences between (i)–(iii) and (i')–(iii') are of a *qualitative character* and, therefore, they cannot be clarified within the framework of assumptions (a)–(d). Because (b) and (d) remain true in these model tests, (a) or/and (c) must be relaxed to explain the differences.

When the Bond number $Bo = g\rho L^2/T_s$ (g is the gravity acceleration, ρ is the liquid density, T_s is the surface tension) is larger than $\sim 10^3$, the surface tension should not affect, globally, the liquid sloshing dynamics (see, page 125 in Faltinsen & Timokha 2009). The capillarity can only influence a local flow at the capillary meniscus due to, e.g., the dynamic contact angle effect, which is, according to Shukhmurzaev (1997), a nonlinear phenomenon. When $10^4 \lesssim Bo = g\rho L^2/T_s$, the surface tension effect can be

fully neglected in the sloshing problems without a gas mixture. Even though Ikeda *et al.* (2012) used a relatively-small laboratory tank with a 0.1×0.1 m square base, computing the Bond number shows that it satisfies the first condition, $10^3 \lesssim Bo$ for the tap water at 20^o C with $T_s = 0.073$ N/m, $\rho = 10^3$ kg/m^3 and $g = 9.81$ m/s^2. As a consequence, assumption (c) is relevant for this experimental case.

Neglecting the linear viscous damping (assumption a) is rather disputable for small-size tanks. According to Keulegan (1959), the linear laminar viscous boundary layer damping ratio for a given natural sloshing mode in a rectangular tank with fixed width-to-breadth ratio and liquid depth-to-tank breadth ratio decreases with increasing the breadth L as $1/L^{3/4}$ (see, also, a discussion on pages 264-265 by Faltinsen & Timokha 2009). Keulegan (1959) showed experimentally an extra non-negligible contribution due to the dynamic contact angle effect. Hence, when $10^3 \lesssim Bo \lesssim 10^4$, the surface tension quantities can be omitted in the dynamic boundary condition but the related damping may matter. Whether the linear viscous damping indeed matters and clarifies the experimental data by Ikeda *et al.* (2012) is a *particular problem*, which will be examined in the present paper by both including the linear viscous damping terms into the Narimanov-Moiseev–type nonlinear multimodal theory of Part 1 and carrying out the corresponding steady-state resonant sloshing analysis.

By writing the present paper, we suggest the three following generalisations of Part 1 in mind. *First*, the steady-state *undamped* sloshing analysis is extended to the case of an arbitrary horizontal *oblique* harmonic excitation. This includes constructing an analytical periodic solution of the Narimanov-Moiseev–type modal system and studying its stability. What happens with the effective frequency ranges for the stable steady-state wave regimes and the corresponding response curves is examined versus the forcing direction, which changes from longitudinal to diagonal one. *Secondly*, we introduce the linear damping terms in the asymptotic modal system and study how this may change the steady-state resonant sloshing. We show that the linear damping leads to a *qualitatively* other steady-state resonant sloshing and prove that (i')–(iii') can replace (i)–(iii). According to our asymptotic theory, this happens when the introduced damping coefficients in the governing equations of the primary-excited sloshing modes are of the order $O(\eta^{2/3})$. Such a damped sloshing is relevant for a relatively small laboratory tank (Ducci & Weheliye 2014). The results can also be useful, e.g. for modelling the sloshing effect in the tetra-pack–type cardboard cartons that are filled by a Newtonian liquid (milk, juice, etc.) in the packing machines (Grundelius 2001). *Thirdly*, we study a complex (double) effect of the linear damping and the forcing direction on the steady-state response curves. Even though the numerical examples were done for the liquid depth-to-tank width ratio $h/L = 0.6$, the results should be qualitatively the same for $0.5 \lesssim h/L$ since the hydrodynamic coefficients in the Narimanov-Moiseev–type modal system weakly change for these depth. These steady-state results are compared with the measured maximum wave elevations by Ikeda *et al.* (2012). Even though our analytical study can evaluate the phase-lags between the harmonic forcing signal as well as between the Stokes cross-wave components, the analysis of these lags is not reported. The analysis deserves an independent publication, especially, in the context of the angular steady flow phenomenon (V-vortex), which was reported by Royon-Lebeaud *et al.* (2007) for swirling.

In § 2, we introduce preliminaries from Part 1 and write down the nine-dimensional Narimanov-Moiseev–type system of ordinary differential (modal) equations, which are equipped with the linear damping terms associated with the logarithmic decrement of the corresponding natural sloshing modes. An oblique harmonic horizontal tank forcing is considered. Utilising the modal equations suggests a set of asymptotic relations between the nondimensional input parameters on the $\epsilon = O(\eta)$ scale. Accounting for

the linear damping in these equations requires the damping coefficients (rates) satisfying the corresponding asymptotic conditions in terms of η.

Can the latter asymptotic conditions be satisfied for realistic model tests? This query is answered in § 3. We utilise the modified Keulegan's formula by Faltinsen & Timokha (2009, Eq. (6.140)) to estimate the damping ratios caused by the linear laminar boundary layer on the wetted tank surface. The formula provides the lowest-order asymptotic approximation in terms of the small parameter $\sqrt{\nu T_{i,j}/L^2}$ (ν is the kinematic viscosity and $T_{i,j}$ is the natural period of the i,j-mode). Computations for the tap water at 20^o C show that the theoretical nondimensional damping coefficients have similar order for the nine lowest natural sloshing modes (governed by the multimodal equations). Because the theoretical damping ratios increase with decreasing L, the required asymptotic condition for the nondimensional damping coefficients cannot be satisfied for larger containers alike in the experiments of Part 1 ($L = 1$ m). For the laboratory tests by Ikeda *et al.* (2012) with the relatively-small 0.1×0.1 m base container, one should recall the experimental results by Keulegan (1959) and Henderson & Miles (1994) (see, also, discussion on pages 264-265 by Faltinsen & Timokha 2009) who pointed out that the linear boundary layer estimate by Faltinsen & Timokha (2009, Eq. (6.140)) gives only a *lower bound* of the linear damping ratios for $L \lesssim 0.2$ m. The difference between the theoretical and measured values can be significant so that, for instance, the computed nondimensional damping coefficient for the first natural sloshing mode in the 0.1×0.1 m tank is equal to 0.01 while Ikeda *et al.* (2012) measured it to be about 0.0256. The latter value can be assumed to be of the required $O(\eta^{2/3})$ order in the model tests by Ikeda *et al.* (2012) where $\eta \approx 0.0075$.

An asymptotic steady-state (periodic) solution of the nonlinear Narimanov-Moiseev–type multimodal system with linear damping terms is analytically derived in § 4 for an arbitrary oblique harmonic forcing. The derivation leads to a *secular* (solvability) *system* of nonlinear algebraic equations, which couples the four lowest $O(\eta^{1/3})$-order amplitude parameters. The multi-timing technique from Part 1 is generalised to study *stability* of the derived steady-state solution. Part 1 shows how to get an analytical solution of the secular system with the zero-damping terms for both longitudinal and diagonal excitations. This analytical scheme is, in our opinion, not applicable for the oblique forcing and/or the non-zero damping.

Because the linear damping causes the two phase-lags ψ and φ for the two lowest-order periodic sloshing components (the components are associated with the perpendicular Stokes modes), a more physically-relevant form of the secular equations, which couples the two amplitudes A, B and the pair ψ, φ for the two Stokes modes, is needed. Such a secular system is derived in § 5. We show that the steady-state resonant sloshing implies a standing wave, if and only if, $\sin(\varphi - \psi) = 0$. Furthermore, we construct an *analytical solution* of the new secular equations for the *undamped* case and an arbitrary (oblique) forcing direction. The solution shows that the oblique forcing theoretically causes maximum six different standing resonant waves and up to three different swirling modes for a fixed forcing frequency. Each swirling mode implies two physically-identical angularly progressive waves in clock- and counterclockwise directions, respectively.

The authors do not know how to construct an analytical solution of the secular equations for the damped resonant sloshing, except for the longitudinal forcing (this solution is derived and presented). However, without such a solution and extensive numerical experiments, we prove in section 5.3 a series of specific qualitative properties regarding the secular equations, which make it possible to confirm that (i')–(iii') indeed replace (i)–(iii) when damping matters. An important conclusion is that the damped sloshing formally makes impossible the squares-like regime and any other standing resonant waves. However, because the standing wave criterion admits an asymptotic

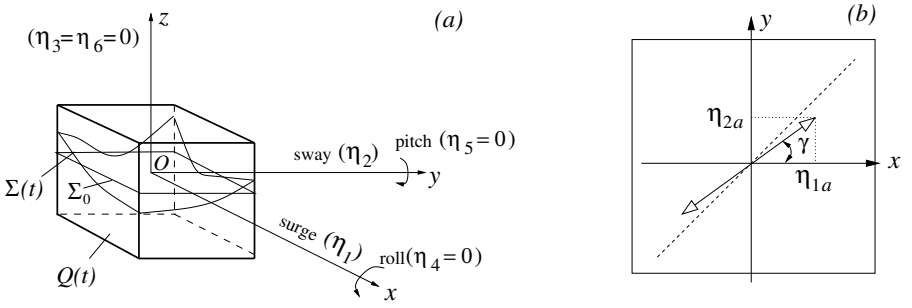

FIGURE 1. The horizontally-excited tank in panel (a). Panel (b) shows the excitation direction with the nondimensional forcing amplitude $\eta = \sqrt{\eta_{1a}^2 + \eta_{2a}^2}$ whose projections on the coordinate axes are $\eta_{1a} = \eta\cos\gamma$ and $\eta_{2a} = \eta\sin\gamma$, $0 \leqslant \gamma \leqslant \pi/4$.

interpretation, $\sin(\varphi - \psi) = O(\eta^{1/3})$, one can introduce an *almost standing* wave mode for certain input parameters. This occurs when one from the two modified Stokes modes, which constitute swirling, has an asymptotically-dominant character. These waves were discovered in the experiments by Ikeda *et al.* (2012, Fig. 4).

In § 6, we conduct a set of computations to examine the evolution of the *undamped* and *damped response* curves versus the angle $0 \leqslant \gamma \leqslant \pi/4$ between the excitation direction and the Ox axis ($\gamma = 0$ corresponds to the longitudinal forcing). The branching for the damped case is similar to that by Ikeda *et al.* (2012) who adopted another adaptive-type modal equations. Difference between damped and undamped branchings can be significant for the oblique (diagonal) forcing. However, the frequency ranges, where all the steady-state wave regimes are unstable and irregular motions occur, undergo insignificant changes. The damping significantly influences the branching for swirling.

In § 7, we compare our theoretical predictions of the maximum wave elevations (the damped sloshing) with experimental measurements by Ikeda *et al.* (2012). The agreement looks rather favourable except, probably, for the larger-amplitude swirling mode. The latter discrepancy can be lowered by adopting a speculatively larger damping ratios as it was done by Ikeda *et al.* (2012).

2. Statement of the problem

We follow Part 1 and consider a rigid square base tank, which is partially filled with an incompressible liquid to the mean liquid depth h. The tank *oscillates harmonically and horizontally* by surge $\eta_1(t) = L\eta_{1a}\cos(\sigma t)$ and sway $\eta_2(t) = L\eta_{2a}\cos(\sigma t)$, where L is the square base side and the nondimensional forcing amplitudes are small and associated with a small input parameter $\epsilon \sim \eta$, i.e.

$$\sqrt{\eta_{1a}^2 + \eta_{2a}^2} = \eta = O(\epsilon) \ll 1.$$

The liquid motions are considered in the tank-fixed coordinate system $Oxyz$ so that the mean free surface Σ_0 belongs to the Oxy plane and Oz passes through the centre of Σ_0 (figure 1). The free surface $\Sigma(t) : z = f(x, y, t)$ and the absolute velocity potential $\Phi(x, y, z, t)$ must simultaneously be found from the corresponding free-surface problem or its variational analogy (see, Chs. 2, 7, and 9 by Faltinsen & Timokha 2009). The *steady-state resonant waves* are described by solutions, which satisfy the periodicity condition $f(x, y, t + 2\pi/\sigma) = f(x, y, t)$ and $\Phi(x, y, z, t + 2\pi/\sigma) = \Phi(x, y, z, t)$.

Furthermore, the forcing frequency σ is close to the lowest natural sloshing frequency $\sigma_1 = \sigma_{0,1} = \sigma_{1,0}$ (corresponds to the two longest Stokes cross-waves) taken from the

infinite set

$$\sigma_{i,j}^2 = \frac{g\pi}{L}\sqrt{i^2+j^2}\,\tanh\left(\frac{\pi\sqrt{i^2+j^2}\,h}{L}\right) \tag{2.1}$$

(Ch. 4 by Faltinsen & Timokha 2009).

To get a *nondimensional formulation*, we adopt the characteristic size L and the characteristic time $1/\sigma_1$. This implies, in particular, the unit breadth = width for the nondimensional tank and the normalised natural sloshing frequencies and the forcing frequency are

$$\bar\sigma_{i,j} = \frac{\sigma_{i,j}}{\sigma_1} \quad \text{and} \quad \bar\sigma = \frac{\sigma}{\sigma_1}, \tag{2.2}$$

respectively.

Adopting the nonlinear multimodal method for the nondimensional sloshing problem suggests the Fourier presentation of the free surface

$$z = f(x,y,t) = \sum_{i,j\geqslant 0, i+j\neq 0} \beta_{i,j}(t)\,\left(f_i^{(1)}(x) f_j^{(2)}(y)\right), \tag{2.3}$$

where $(f_i^{(1)}(x)\, f_j^{(2)}(y))$ are the nondimensional natural sloshing modes,

$$f_i^{(1)}(x) = \cos(\pi i(x+\tfrac{1}{2})), \quad f_i^{(2)}(y) = \cos(\pi i(y+\tfrac{1}{2})), \quad i \geqslant 0, \tag{2.4}$$

corresponding to the natural sloshing frequencies (2.1) and $\beta_{i,j}(t)$ are the *sloshing-related generalised coordinates*.

Part 1 derived the Narimanov-Moiseev–type nonlinear (asymptotic) modal system coupling $\beta_{i,j}(t)$, which takes, after re-denoting $\beta_{1,0} = a_1, \beta_{2,0} = a_2, \beta_{0,1} = b_1, \beta_{0,2} = b_2, \beta_{1,1} = c_1, \beta_{3,0} = a_3, \beta_{2,1} = c_{21}, \beta_{1,2} = c_{12}, \beta_{0,3} = b_3$, the form

$$\ddot a_1 + \boxed{2\xi_{1,0}\dot a_1} + a_1 + d_1(\ddot a_1 a_2 + \dot a_1\dot a_2) + d_2(\ddot a_1 a_1^2 + \dot a_1^2 a_1) + d_3\ddot a_2 a_1 + d_6\ddot a_1 b_1^2 + d_9\ddot c_1 b_1$$
$$+ \ddot b_1(d_7 c_1 + d_8 a_1 b_1) + d_{10}\dot b_1^2 a_1 + d_{11}\dot a_1\dot b_1 b_1 + d_{12}\dot b_1\dot c_1 = P_{1,0}\eta_{1a}\bar\sigma^2\cos(\bar\sigma t), \quad (2.5a)$$

$$\ddot b_1 + \boxed{2\xi_{0,1}\dot b_1} + b_1 + d_1(\ddot b_1 b_2 + \dot b_1\dot b_2) + d_2(\ddot b_1 b_1^2 + \dot b_1^2 b_1) + d_3\ddot b_2 b_1 + d_6\ddot b_1 a_1^2 + d_9\ddot c_1 a_1$$
$$+ \ddot a_1(d_7 c_1 + d_8 a_1 b_1) + d_{10}\dot a_1^2 b_1 + d_{11}\dot a_1\dot b_1 a_1 + d_{12}\dot a_1\dot c_1 = P_{0,1}\eta_{2a}\bar\sigma^2\cos(\bar\sigma t), \quad (2.5b)$$

$$\ddot a_2 + \boxed{2\xi_{2,0}\bar\sigma_{0,2}\dot a_2} + \bar\sigma_{2,0}^2 a_2 + d_4\ddot a_1 a_1 + d_5\dot a_1^2 = 0; \tag{2.5c}$$

$$\ddot b_2 + \boxed{2\xi_{0,2}\bar\sigma_{0,2}\dot b_2} + \bar\sigma_{0,2}^2 b_2 + d_4\ddot b_1 b_1 + d_5\dot b_1^2 = 0, \tag{2.5d}$$

$$\ddot c_1 + \boxed{2\xi_{1,1}\bar\sigma_{1,1}\dot c_1} + \bar\sigma_{1,1}^2 c_1 + \hat d_1\ddot a_1 b_1 + \hat d_2\ddot b_1 a_1 + \hat d_3\dot a_1\dot b_1 = 0, \tag{2.5e}$$

$$\ddot a_3 + \boxed{2\xi_{3,0}\bar\sigma_{3,0}\dot a_3} + \bar\sigma_{3,0}^2 a_3 + \ddot a_1(q_1 a_2 + q_2 a_1^2) + q_3\ddot a_2 a_1 + q_4\dot a_1^2 a_1 + q_5\dot a_1\dot a_2$$
$$= P_{3,0}\eta_{1a}\bar\sigma^2\cos(\bar\sigma t), \quad (2.6a)$$

$$\ddot c_{21} + \boxed{2\xi_{2,1}\bar\sigma_{2,1}\dot b_3} + \bar\sigma_{2,1}^2 c_{21} + \ddot a_1(q_6 c_1 + q_7 a_1 b_1) + \ddot b_1(q_8 a_2 + q_9 a_1^2) + q_{10}\ddot a_2 b_1 + q_{11}\ddot c_1 a_1$$
$$+ q_{12}\dot a_1^2 b_1 + q_{13}\dot a_1\dot b_1 a_1 + q_{14}\dot a_1\dot c_1 + q_{15}\dot a_2\dot b_1 = 0, \quad (2.6b)$$

$$\ddot c_{12} + \boxed{2\xi_{1,2}\bar\sigma_{1,2}\dot b_3} + \bar\sigma_{1,2}^2 c_{12} + \ddot b_1(q_6 c_1 + q_7 a_1 b_1) + \ddot a_1(q_8 b_2 + q_9 b_1^2) + q_{10}\ddot b_2 a_1 + q_{11}\ddot c_1 b_1$$

$$+ q_{12}\dot{b}_1^2 a_1 + q_{13}\dot{a}_1\dot{b}_1 b_1 + q_{14}\dot{b}_1\dot{c}_1 + q_{15}\dot{a}_1\dot{b}_2 = 0, \quad (2.6c)$$

$$\ddot{b}_3 + \boxed{2\xi_{0,3}\bar{\sigma}_{0,3}\dot{b}_3} + \bar{\sigma}_{0,3}^2 b_3 + \ddot{b}_1(q_1 b_2 + q_2 b_1^2) + q_3\ddot{b}_2 b_1 + q_4\dot{b}_1^2 b_1 + q_5\dot{b}_1\dot{b}_2$$
$$= P_{0,3}\eta_{2a}\bar{\sigma}^2\cos(\bar{\sigma}t); \quad (2.6d)$$

where

$$P_{i,0} = P_{0,i} = \frac{2}{\pi i}\left[(-1)^i - 1\right]\tanh(\pi i h/L), \quad (2.7)$$

Part 1 also gives explicit expressions for the hydrodynamic coefficients at the nonlinear terms, which are also computed in Faltinsen & Timokha (2009, Tables 9.1-9.2).

The derivation details and applicability limits of the nonlinear asymptotic modal system (2.5)-(2.6) are extensively discussed in Part 1. The system requires that (a) the nondimensional forcing amplitude is small, (b) the forcing frequency σ is close to the lowest natural sloshing frequency σ_1 ($\bar{\sigma}$ satisfies the Moiseev detuning), (c) the two lowest perpendicular Stokes modes (associated with the generalised coordinates $a_1(t)$ and $b_1(t)$) give the lowest-order (dominant) asymptotic contribution $O(\eta^{1/3}) = O(\epsilon^{1/3})$, and (d) there are no secondary resonances.

The actual asymptotic ordering of the higher sloshing modes (generalised coordinates) are *mathematically* deduced following the Narimanov-Moiseev asymptotic technique, which proves that the second order modes are exclusively associated with a_2, b_2 and c_1 but c_{12}, c_{21}, a_3 and b_3 are of the third order on the $\epsilon = O(\eta) \ll 1$ scale. The Narimanov–Moiseev-type modal system may fail with decreasing the liquid depth, increasing the forcing amplitude and for the transient sloshing. Physically, this is due to the secondary resonance phenomenon. The multimodal analysis needs then the so-called adaptive ordering whose concept was elaborated by Faltinsen *et al.* (2005*b*, 2006*b*). In the corresponding adaptive modal systems, the higher-order generalised coordinates, including a_2, b_2, c_1 and c_{12}, c_{21}, a_3, b_3 as well as generalised coordinates, which are not accounted for by the Narimanov–Moiseev asymptotic scheme, can contribute to the lower asymptotic components (Faltinsen *et al.* 2005*b*, 2006*b*). A version of the adaptive modal ordering was adopted by Ikeda *et al.* (2012), probably, to improve agreement with experiments for transients; they used a direct simulation of transient and steady-state waves (combined with a path-following procedure) to numerically analyse the steady-state regimes and their stability.

For the oblique forcing in figure 1 (b), the assumptions (a-d) can be mathematically formalised as

$$\eta_{2a} = \delta\eta_{1a}, \quad 0 \leqslant \delta = \tan\gamma \leqslant 1; \quad 0 < \epsilon = P_1\eta_{1a} = -P_{1,0}\eta_{1a} = O(\eta), \quad (2.8a)$$

$$\Lambda = (\sigma_1/\sigma)^2 - 1 = \bar{\sigma}^{-2} - 1 = O(\epsilon^{2/3}) \ \text{(the Moiseev detuning)}, \quad (2.8b)$$

$$a_1 \sim b_1 = O(\epsilon^{1/3}) \quad \Rightarrow \quad a_2 \sim b_2 \sim c_1 = O(\epsilon^{2/3}) \ \&\ a_3 \sim b_3 \sim c_{21} \sim c_{12} = O(\epsilon), \quad (2.8c)$$

$$\bar{\sigma}_{0,2}^2 - 4 = O(1), \quad \bar{\sigma}_{1,1}^2 - 4 = O(1), \quad \bar{\sigma}_{0,3}^2 - 9 = O(1), \quad \bar{\sigma}_{1,2}^2 - 9 = O(1). \quad (2.8d)$$

3. Linear viscous damping ratios

Because (2.5)–(2.6) suggests neglecting the $o(\epsilon)$-terms, the nondimensional damping coefficients at the linear framed terms should possess the asymptotic conditions

$$2\xi_{1,0} = 2\xi_{0,1} = O(\epsilon^{2/3}); \ \ 2\xi_{i,j}\bar{\sigma}_{i,j} = O(\epsilon^{1/3}), \ i+j=2; \ \ 2\xi_{i,j}\bar{\sigma}_{i,j} = O(1), \ i+j=3 \ \ (3.1)$$

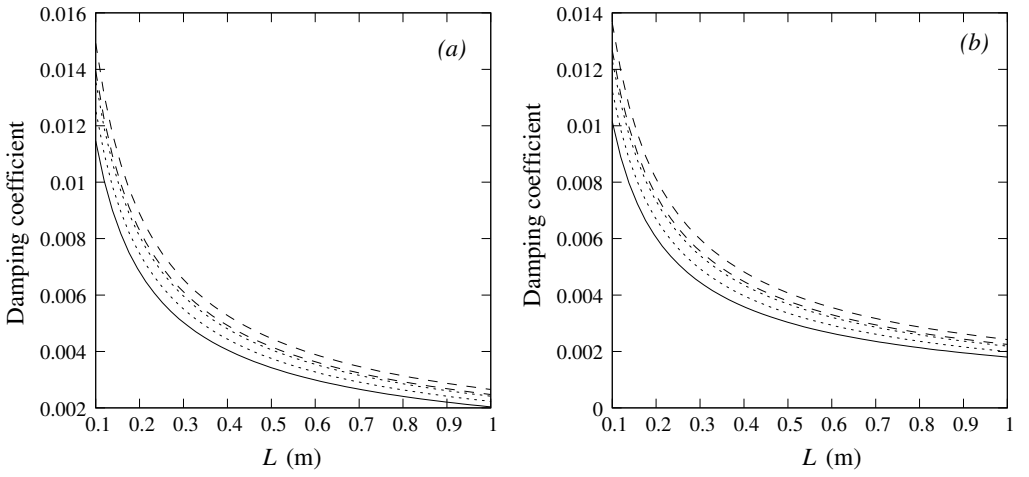

FIGURE 2. The theoretical nondimensional damping coefficients $2\xi_{i,j}\bar{\sigma}_{i,j}$ in the framed terms of the modal equations (2.5)-(2.6) *versus* the tank breadth = width L (m). The values are computed by (3.3) for the tap water with $\nu = 10^{-6}$ [m^2/s]. The solid line corresponds to $\xi = 2\xi_{0,1} = 2\xi_{1,0}$, the dotted lines imply $2\xi_{2,0}\bar{\sigma}_{2,0}$ and $2\xi_{1,1}\bar{\sigma}_{1,1}$ and the dashed lines are used to mark $2\xi_{3,0}\bar{\sigma}_{3,0}$ and $2\xi_{2,1}\bar{\sigma}_{2,1}$. The panel (a) is drawn for $h/L = 0.35$ and (b) is for $h/L = 0.6$. The damping coefficients have the asymptotic $L^{-3/4}$.

to be accounted for simultaneously. Because a_1 and b_1 have a dominant character, one should concentrate on

$$\xi = 2\xi_{1,0} = O(\epsilon^{2/3}) \tag{3.2}$$

for the lowest order Stokes modes governed by (2.5).

The linear damping for sloshing in a clean tank is extensively discussed in Faltinsen & Timokha (2009, ch. 6). The damping ratios $\xi_{i,j}$ are associated with the logarithmic decrements of the natural sloshing modes whose primary contribution is caused by the linear boundary layer at the wetted tank surface. Faltinsen & Timokha (2009, Eq. (6.140)) gives the asymptotic approximation

$$\xi_{i,j} = \sqrt{\frac{\nu}{2L^2\sigma_{i,j}}}\left[3 + 2\pi\frac{\sqrt{i^2+j^2}\,(0.5 - h/L)}{\sinh(2\pi\sqrt{i^2+j^2}\,h/L)}\right] \tag{3.3}$$

in terms of $\sqrt{\nu/(2L^2\sigma_{i,j})} \ll 1$, where ν is the kinematic viscosity coefficient. As discussed by Keulegan (1959) and Faltinsen & Timokha (2009, Sect. 6.3.1), (3.3) provides a rather accurate estimate of the damping ratios for the lower natural sloshing modes in a relatively large rectangular tank. When $L \lesssim 0.2$ m, the experimental damping ratios may be larger than this theoretical value. Keulegan (1959) explained this fact by the dynamic contact angle (meniscus) effect. He illustrated his hypothesis by comparing the damping ratios for Lucite and glass basins (see, Fig. 6.6 by Faltinsen & Timokha 2009), which are clearly different and larger than the estimate (3.3). The higher experimental damping ratios for the relatively small tanks were described by Henderson & Miles (1994) and Ikeda *et al.* (2012) ($L = 0.1$ m and $h/L = 0.6$). Ikeda *et al.* (2012) reported the experimental value $\xi = 2 \cdot 0.0128 = 0.0256$ while (3.3) computes $\xi = 2\xi_{1,0} = 0.01$.

The nondimensional damping coefficients $2\xi_{i,j}\bar{\sigma}_{i,j}$ for a tap water with $\nu = 10^{-6}$ m^2/s are computed in figure 2 versus the tank breadth = width L (m) for $h/L = 0.35$ and 0.6. The solid lines correspond to $\xi = 2\xi_{0,1} = 2\xi_{1,0}$, the dotted lines imply $2\xi_{2,0}\bar{\sigma}_{2,0}$ and $2\xi_{1,1}\bar{\sigma}_{1,1}$ and the dashed lines are used to mark $2\xi_{3,0}\bar{\sigma}_{3,0}$ and $2\xi_{2,1}\bar{\sigma}_{2,1}$. The figure

shows that the relative difference between these lines is not large and the computed nondimensional damping coefficients for the considered nine sloshing modes have similar asymptotic order. As a consequence, (3.1) cannot be satisfied for all damping coefficients. One should focus on (3.2) for a_1 and b_1, but neglect the linear damping terms for the higher-order generalised coordinates in (2.5*c*)-(2.6).

In Part 1 and Ikeda *et al.* (2012), the nondimensional experimental amplitudes were about $O(\epsilon) = \eta = 0.0075$ (actually, 0.0078 and 0.00725). The first tank has the horizontal dimension $L = 1$ m. For this size, (3.3) provides a rather accurate prediction of ξ. Figure 2 shows that $\xi = 0.002 < \eta$ in this case so that the asymptotic condition (3.2) is clearly *unsatisfied*. For the laboratory tank ($L = 0.1$ m) by Ikeda *et al.* (2012), the theoretical damping coefficient is $\xi = 0.01$ but the authors reported the experimental $\xi = 0.0256$. This value may theoretically be considered as satisfying (3.2) for $\eta = 0.0075$.

4. Steady-state asymptotic solution and its stability

By applying the analytical scheme by Faltinsen *et al.* (2003, Sect. 3.2), one can derive an *exact asymptotic steady-state solution* of (2.5)-(2.6) starting with

$$a_1(t) = a\cos\bar{\sigma}t + \bar{a}\sin\bar{\sigma}t + o(\epsilon^{1/3}); \quad b_1(t) = \bar{b}\cos\bar{\sigma}t + b\sin\bar{\sigma}t + o(\epsilon^{1/3}), \tag{4.1}$$

which determines the *lowest-order approximation of the surface wave*

$$z = S(x,y;a,\bar{b})\cos\bar{\sigma}t + S(x,y;\bar{a},b)\sin\bar{\sigma}t + o(\epsilon^{1/3}), \tag{4.2}$$

where $S(x,y;a,b) = af_1^{(1)}(x) + bf_1^{(2)}(y)$ is the combined Stokes mode.

The derivation is presented in Appendix A. The asymptotic procedure is almost identical to that from Part 1. We neglect the linear damping terms in (2.5*c*) (see, discussion in § 3). The third-order generalised coordinates by (2.6) are driven. They do not affect a_1, b_1, a_2, b_2 and c_1. We arrive at the necessary solvability condition appearing as the (secular) system of nonlinear algebraic equations

$$\begin{cases} ① : a\left[\Lambda + m_1(a^2+\bar{a}^2) + m_2\bar{b}^2 + m_3b^2\right] + \bar{a}\left[(m_2-m_3)\bar{b}b + \xi\right] = \epsilon, \\ ② : \bar{a}\left[\Lambda + m_1(a^2+\bar{a}^2) + m_2b^2 + m_3\bar{b}^2\right] + a\left[(m_2-m_3)\bar{b}b - \xi\right] = 0, \\ ③ : b\left[\Lambda + m_1(b^2+\bar{b}^2) + m_2\bar{a}^2 + m_3a^2\right] + \bar{b}\left[(m_2-m_3)\bar{a}a - \xi\right] = 0, \\ ④ : \bar{b}\left[\Lambda + m_1(b^2+\bar{b}^2) + m_2a^2 + m_3\bar{a}^2\right] + b\left[(m_2-m_3)\bar{a}a + \xi\right] = \delta\epsilon, \end{cases} \tag{4.3}$$

which couples the nondimensional amplitude parameters $a, \bar{a}, b$ and $\bar{b}$. The right-hand side components are defined by (2.8*a*). The coefficients m_1 and m_3 are strongly affected by the second-order generalised coordinates by (2.5*c*), so that

$$\begin{aligned} m_1 &= -\tfrac{1}{2}d_2 - d_1(p_0 - \tfrac{1}{2}h_0) - 2h_0d_3, \\ m_2 &= -\tfrac{3}{4}d_6 + \tfrac{1}{4}d_{10} - \tfrac{3}{4}d_8 + \tfrac{1}{4}d_{11} - d_7p_1 - h_1(\tfrac{1}{2}d_7 + 2d_9 - d_{12}), \\ m_3 &= -\tfrac{1}{4}d_6 + \tfrac{3}{4}d_{10} - \tfrac{1}{4}d_8 - \tfrac{1}{4}d_{11} - h_1(\tfrac{1}{2}d_7 + 2d_9 - d_{12}) \end{aligned}$$

and $\xi = 2\xi_{0,1} = 2\xi_{1,0}$, which are functions of the nondimensional liquid depth h/L. Owing to (2.8*b*) and (3.2), all quantities in (4.3) have the same asymptotic order $O(\epsilon)$. The functions $m_i = m_i(h/L)$ were analysed in Part 1 (see, figure 3). The graphs show that $m_2 < 0$, $h/L > 0.17...$, $m_1 + m_2 < 0$ for $h/L > 0.27...$ and $m_2 - m_3 < 0$, $m_1 + m_3 > 0$ for the finite liquid depths, $0.5 \lesssim h/L$. We use these inequalities in our forthcoming analytical and numerical studies and, therefore, these are, generally speaking, restricted to $0.5 \lesssim h/L$.

We can use the linear Lyapunov method and the multi-timing technique to study

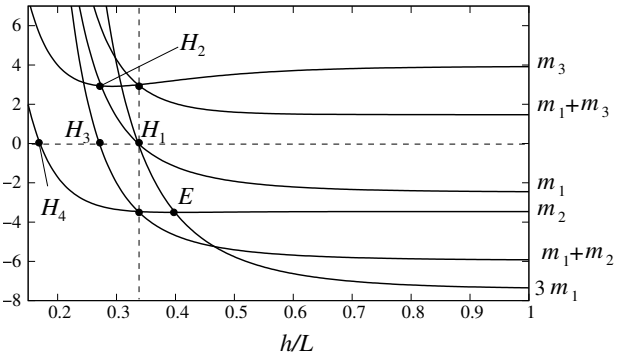

FIGURE 3. Reprint from Faltinsen *et al.* (2003, Fig. 4) illustrating the nondimensional coefficients $m_i(h/L)$, $i = 1, 2, 3$ and their linear combinations *versus* the liquid-depth-to-breadth ratio h/L for a square base basin. The point $H_1\,(m_1 = 0, h/L = 0.337...)$ denotes the soft/hard spring change for the planar steady-state waves. The point $H_2\,(m_1 = m_3)$ defines $h/L = 0.274...$, H_3 implies $h/L = 0.27...$, where $m_1 + m_2 = 0$, and H_4 corresponds to $h/L = 0.17...$, where $m_2 = 0$. The point $E\,(h/L = 0.4...)$ is obtained from the equality $m_2 = 3m_1$.

the stability of the constructed asymptotic steady-state solutions. For this purpose, we introduce the slowly varying time $\tau = \frac{1}{2}\epsilon^{2/3}\bar{\sigma}t$, whose order is chosen according to the Moiseyev detuning $\bar{\sigma}^{-2} - 1 = O(\epsilon^{2/3})$, and express the perturbed solutions as

$$\begin{aligned} a_1 &= (a + \alpha(\tau))\cos\bar{\sigma}t + (\bar{a} + \bar{\alpha}(\tau))\sin\bar{\sigma}t + o(\epsilon^{1/3}),\\ b_1 &= (\bar{b} + \bar{\beta}(\tau))\cos\bar{\sigma}t + (b + \beta(\tau))\sin\bar{\sigma}t + o(\epsilon^{1/3}), \end{aligned} \tag{4.4}$$

where $a, \bar{a}, b$ and $\bar{b}$ come from (4.3). Inserting (4.4) into (2.5)-(2.6), gathering terms of the lowest asymptotic quantities order and keeping linear terms in $\alpha, \bar{\alpha}, \beta$ and $\bar{\beta}$ lead to the following linear system of ordinary differential equations

$$\mathbf{s}' + \xi\mathbf{s} + \mathcal{S}\,\mathbf{s} = 0, \tag{4.5}$$

where $\mathbf{s} = (\alpha, \bar{\alpha}, \beta, \bar{\beta})^T$, the prime is the differentiation by τ, and the matrix $\mathcal{S}$ has the following elements

$$\begin{aligned}
&s_{11} = -2m_1a\bar{a} - (m_2 - m_3)b\bar{b};\quad s_{12} = -\Lambda - m_1a^2 - 3m_1\bar{a}^2 - m_2b^2 - m_3\bar{b}^2,\\
&s_{13} = -2m_2\bar{a}b - (m_2 - m_3)a\bar{b};\quad s_{14} = -2m_3\bar{a}\bar{b} - (m_2 - m_3)ab,\\
&s_{21} = \Lambda + 3m_1a^2 + m_1\bar{a}^2 + m_2\bar{b}^2 + m_3b^2;\quad s_{22} = 2m_1a\bar{a} + (m_2 - m_3)b\bar{b},\\
&s_{23} = 2m_3ab + (m_2 - m_3)\bar{a}\bar{b};\quad s_{24} = 2m_2a\bar{b} + (m_2 - m_3)\bar{a}b,\\
&s_{31} = 2m_2a\bar{b} + (m_2 - m_3)b\bar{a};\quad s_{32} = 2m_3\bar{a}\bar{b} + (m_2 - m_3)ab,\\
&s_{33} = 2m_1b\bar{b} + (m_2 - m_3)a\bar{a};\quad s_{34} = \Lambda + m_1b^2 + 3m_1\bar{b}^2 + m_2a^2 + m_3\bar{a}^2,\\
&s_{41} = -2m_3ab - (m_2 - m_3)\bar{a}\bar{b};\quad s_{42} = -2m_2\bar{a}b - (m_2 - m_3)a\bar{b},\\
&s_{43} = -\Lambda - 3m_1b^2 - m_1\bar{b}^2 - m_2\bar{a}^2 - m_3a^2;\quad s_{44} = -2m_1b\bar{b} - (m_2 - m_3)a\bar{a}.
\end{aligned}$$

The fundamental solution $\mathbf{s} = \exp(\lambda\tau)\mathbf{a}$ of (4.5) follows from the spectral matrix problem $[(\lambda + \xi)E + S]\mathbf{a} = 0$, where λ are the unknown eigenvalues and $\mathbf{a}$ are the corresponding eigenvectors. Computations give the following characteristic bi-quadratic equation

$$(\lambda + \xi)^4 + s_1(\lambda + \xi)^2 + s_0 = 0, \tag{4.6}$$

where s_0 is the determinant of $\mathcal{S}$ and s_1 is a complicated function of the elements of $\mathcal{S}$. The eigenvalues λ can be expressed as $-\xi \pm \sqrt{x_{1,2}}$, where $x_{1,2} = \frac{1}{2}(-s_1 \pm \sqrt{s_1^2 - 4s_0})$

are two solutions of the quadratic equation $x^2 + s_1 x + s_0 = 0$. The fixed-point solution (associated with $a, \bar{a}, b$ and $\bar{b}$) is asymptotically stable ($\alpha, \bar{\alpha}, \beta$ and $\bar{\beta}$ exponentially decay with τ) if and only if the real component of λ is strongly negative.

In the limit case $\xi \to 0$, Part 1 derived the stability condition ($\Re[\lambda] < 0$) in the following form

$$s_1^2 - 4s_0 \geqslant 0 \quad \& \quad s_0 \geqslant 0 \quad \& \quad s_1 \geqslant 0. \tag{4.7}$$

For $O(\epsilon^{2/3}) = \xi > 0$, the stability condition can be written as the alternative

$$\begin{aligned} &\text{either} \quad s_1^2 - 4s_0 \geqslant 0 \;\&\; -s_1 + \sqrt{s_1^2 - 4c_s} \leqslant 0 \quad (\Leftrightarrow s_0 \geqslant 0 \;\&\; s_1 \geqslant 0)\,, \\ &\quad \text{or} \quad s_1^2 - 4s_0 \geqslant 0 \;\&\; -s_1 + \sqrt{s_1^2 - 4s_0} > 0 \;\&\; \sqrt{\tfrac{1}{2}\left(-s_1 + \sqrt{s_1^2 - 4s_0}\right)} < \xi, \\ &\quad \text{or} \quad s_1^2 - 4s_0 < 0 \;\&\; \sqrt{2\sqrt{s_0} - s_1} < \xi. \end{aligned} \tag{4.8}$$

Part 1 constructed an analytical solution of (4.3) for the undamped sloshing with $\xi = 0$ and either longitudinal ($\delta = 0$) or diagonal ($\delta = 1$) excitation. The proposed analytical technique is most probably not applicable for oblique forcing directions with $0 < \delta < 1$ as well as for the damped case with $\xi = O(\epsilon^{2/3})$. The forthcoming section proposes an *alternative analytical approach*.

5. Damped versus undamped sloshing. Qualitative differences

5.1. *Rewriting (4.3) in an alternative form*

The non-zero linear damping naturally leads the two phase-lags, ψ and φ, for the two perpendicular Stokes modes $f_1^{(1)}(x)$ and $f_1^{(2)}(y)$ (along the Ox and Oy directions) in (4.2), which are characterised by the lowest-order amplitude parameters $a, \bar{a}$ and $b, \bar{b}$, respectively. A physically-relevant form of (4.3) should therefore couple the 'integral' lowest-order amplitudes A, B and the phase-lags ψ, φ:

$$A = \sqrt{a^2 + \bar{a}^2} \quad \text{and} \quad B = \sqrt{\bar{b}^2 + b^2} > 0, \tag{5.1a}$$

$$a = A\cos\psi, \quad \bar{a} = A\sin\psi, \quad \bar{b} = B\cos\varphi, \quad b = B\sin\varphi. \tag{5.1b}$$

To get these equations, we insert (5.1) into expressions $\bar{a}\,①\,-\,a\,②$, $\bar{b}\,③\,-\,b\,④$, $a\,①\,+\,\bar{a}\,②$ and $b\,③\,+\,\bar{b}\,④$ of (4.3), which give

$$\begin{cases} \boxed{1}: \; A\,[\Lambda + m_1 A^2 + \mathcal{F} B^2] = \epsilon\cos\psi, & \boxed{3}: \; A\,[\mathcal{D} B^2 + \xi] = \epsilon\sin\psi, \\ \boxed{2}: \; B\,[\Lambda + m_1 B^2 + \mathcal{F} A^2] = \delta\epsilon\cos\varphi, & \boxed{4}: \; B\,[\mathcal{D} A^2 - \xi] = -\delta\epsilon\sin\varphi, \end{cases} \tag{5.2a}$$

$$\begin{aligned} \mathcal{F} &= m_2\cos^2(\alpha) + m_3\sin^2(\alpha) = (m_2 + m_3\,C^2)/(1 + C^2), \\ \mathcal{D} &= (m_3 - m_2)\sin(\alpha)\cos(\alpha) = (m_3 - m_2)\,C/(1 + C^2), \end{aligned} \tag{5.2b}$$

where

$$\alpha = \varphi - \psi, \quad C = \tan\alpha$$

($\mathcal{F}(\alpha)$ and $\mathcal{D}(\alpha)$ are the π-periodic functions of the phase-lags difference α). The secular systems (4.3) and (5.2) are *mathematically equivalent*, i.e., getting known A, B, ψ, φ from (5.2) computes $a, \bar{a}, b, \bar{b}$ and *visa-versa*.

The present paper concentrates on the response curves in the $(\bar{\sigma}, A, B)$ space. To

exclude the phase-lags ψ and φ from (5.2), one can take $\boxed{1}^2+\boxed{3}^2$ and $\boxed{2}^2+\boxed{4}^2$ leading to the two equations with respect to A and B

$$\begin{cases} A^2\left[(\Lambda+m_1A^2+\mathcal{F}B^2)^2+(\mathcal{D}B^2+\xi)^2\right]=\epsilon^2,\\ B^2\left[(\Lambda+m_1B^2+\mathcal{F}A^2)^2+(\mathcal{D}A^2-\xi)^2\right]=\delta^2\epsilon^2,\end{cases} \tag{5.3}$$

which parametrically depend on α (or $C=\tan\alpha$). An additional equation is needed to compute α. Inserting $\varphi=\psi+\alpha$ into $\boxed{2}$ and $\boxed{4}$ and using expressions for $(\epsilon\cos\psi)$ and $(\epsilon\cos\psi)$ from $\boxed{1}$ and $\boxed{3}$ gives

$$\begin{cases} (\delta A)\left[\cos\alpha(\Lambda+m_1A^2+\mathcal{F}B^2)-\sin\alpha(\mathcal{D}B^2+\xi)\right]-B\left[\Lambda+m_1B^2+\mathcal{F}A^2\right]=0,\\ (\delta A)\left[\cos\alpha(\mathcal{D}B^2+\xi)+\sin\alpha(\Lambda+m_1A^2+\mathcal{F}B^2)\right]+B\left[\mathcal{D}A^2-\xi\right]=0,\end{cases} \tag{5.4}$$

which can be treated as a system of linear algebraic homogeneous equations with respect to the amplitude parameters δA and B. When $\delta\neq 0$ (*non-longitudinal* forcing), the system should have a nontrivial solution ($\delta AB\neq 0$) and, therefore, the zero-determinant condition must be satisfied

$$\begin{aligned}&\sin\alpha\left[\Lambda^2+\xi^2+(m_1+m_3)\Lambda(A^2+B^2)+m_1m_3(A^4+B^4)\right.\\ &\quad\left.+A^2B^2(m_1^2+m_3^2-\cos^2\alpha\,(m_2-m_3)^2)\right]+\xi\cos\alpha\,(m_1-m_2)(B^2-A^2)=0.\end{aligned} \tag{5.5}$$

The system (5.3), (5.5) governs A^2, B^2 and α for the *oblique* forcing. When $\delta=0$ (the *longitudinal* forcing), (5.4) leads to the equations

$$B[\Lambda+m_1B^2+\mathcal{F}A^2]=0 \text{ and } \ B[\mathcal{D}A^2-\xi]=0, \tag{5.6}$$

whose solutions are either $B=0$ (a planar wave occurring in the excitation plane Oxz) or $B\neq 0$ (three-dimensional sloshing). The planar standing wave is governed by

$$A^2\left[(\Lambda+m_1A^2)^2+\xi^2\right]=\epsilon^2, \quad B=0 \tag{5.7}$$

but the three-dimensional sloshing follows from the system

$$\begin{cases} A^2\left[(\Lambda+m_1A^2+\mathcal{F}(\alpha)B^2)^2+(\mathcal{D}(\alpha)B^2+\xi)^2\right]=\epsilon^2,\\ \Lambda+m_1B^2+\mathcal{F}(\alpha)A^2=0, \quad \mathcal{D}(\alpha)A^2-\xi=0.\end{cases} \tag{5.8}$$

Remark 1. The steady-state resonant waves by (4.2) *always* imply either standing (the two combined Stokes modes in (4.2) are the same) or swirling wave. A criterion for the standing wave is that vectors $(a,\bar{b})$ and $(\bar{a},b)$ are parallel, i.e.

$$ab=\bar{a}\bar{b}\ \Leftrightarrow\ \sin(\varphi-\psi)=0,\ C=\tan(\varphi-\psi)=0\ \Leftrightarrow\ \varphi=\psi+\pi i,\ \ i=0,\pm1,\pm2,\ldots. \tag{5.9}$$

This means that a standing resonant wave occurs, if and only if, *the phase-lags difference is proportional to* π ($C=0$). Otherwise, (4.2) defines *swirling*.

Remark 2. When $\xi^2+\delta^2\neq 0$ (namely, except for the longitudinally-excited undamped sloshing), $\cos\alpha\neq 0$. Indeed, if $\delta=0$ and $\xi\neq 0$ (longitudinally-excited damped sloshing), owing to (5.9), the phase-lags difference $\alpha=0$ for the planar standing waves ($\Rightarrow\cos\alpha=\pm1$) and the last equation of (5.8), $(m_3-m_2)\cos\alpha\sin\alpha=\xi\neq 0$ does not allow $\cos\alpha=0$ for the three-dimensional sloshing. Furthermore, when $\delta\neq 0$ (oblique excitations), assuming $\cos\alpha=0$ transforms (5.5) to

$$\xi^2=-(\Lambda+m_1A^2+m_3B^2)(\Lambda+m_1B^2+m_3A^2),\ \mathcal{F}=m_3 \text{ and } \mathcal{D}=0. \tag{5.10}$$

Inserting ξ^2 into the two equations of (5.3), multiplying these equations and, again, using

(5.10) derive

$$A^2B^2\xi^2(A^2-B^2)^2(m_1-m_3)=\delta^2\epsilon^4>0,$$

which is never satisfied for $\delta\neq 0$, since $(m_1-m_3)<0$ according to figure 3.

When $\cos\alpha\neq 0$, one can multiply (5.5) by $\cos\alpha$ and rewrite the system (5.3), (5.5) in the form

$$\mathrm{a}_2(C^2+1)+(\mathrm{a}_0-\mathrm{a}_2)+\xi\,\mathrm{a}_1C=0,\quad \mathrm{b}_2(C^2+1)+(\mathrm{b}_0-\mathrm{b}_2)-\xi\,\mathrm{a}_1C=0, \tag{5.11a}$$

$$C\left((C^2+1)\,\mathrm{c}_3+\mathrm{c}_1\right)+\xi\,\mathrm{c}_0\,(1+C^2)=0, \tag{5.11b}$$

where

$$\mathrm{a}_2=A^2\left((\Lambda+m_1A^2+m_3B^2)^2+\xi^2\right)-\epsilon^2;\ \mathrm{b}_2=B^2\left((\Lambda+m_1B^2+m_3A^2)^2+\xi^2\right)-\delta^2\epsilon^2,$$
$$\mathrm{a}_0=A^2\left((\Lambda+m_1A^2+m_2B^2)^2+\xi^2\right)-\epsilon^2;\ \mathrm{b}_0=B^2\left((\Lambda+m_1B^2+m_2A^2)^2+\xi^2\right)-\delta^2\epsilon^2,$$
$$\mathrm{a}_1=(m_3-m_2)A^2B^2,$$
$$\mathrm{c}_3=\xi^2+(\Lambda+m_1A^2+m_3B^2)\,(\Lambda+m_1B^2+m_3A^2),$$
$$\mathrm{c}_1=-(m_3-m_2)^2A^2B^2,\quad \mathrm{c}_0=(m_1-m_2)(B^2-A^2).$$

Remark 3. The coefficients at C and C^2 in (5.11a) have the equal asymptotic order, namely, $\mathrm{b}_2\sim\mathrm{b}_0\sim\mathrm{a}_2\sim\mathrm{a}_0\sim\xi\,\mathrm{a}_1=O(\epsilon^2)$. It can happen that solving the system (5.11) gives a small nonzero C, i.e.

$$0\neq|C|\lesssim O(\epsilon^{1/3})=O(\sqrt{A^2+B^2}). \tag{5.12}$$

Formally, this solution implies a swirling wave mode (Remark 1 above). However, by treating (5.11a) in an asymptotic sense on the $\epsilon^{1/3}$ scale and neglecting the $o(\epsilon^2)$ terms leads to $\mathrm{b}_0=\mathrm{a}_0=0$, which are equations for a standing wave regime. This formal mathematical conflict can be resolved by interpreting (5.12) as a condition for an *almost-standing* wave mode. Ikeda *et al.* (2012, Fig. 4 (g)) experimentally observed those modes.

5.2. *Undamped steady-state resonant sloshing for oblique excitations*

When $0<\delta\leqslant 1\,(0<\gamma\leqslant\pi/4)$, the steady-state analysis can be done by using (5.11) with $\xi=0$, which takes the form

$$\mathrm{a}_2^0(C^2+1)+(\mathrm{a}_0^0-\mathrm{a}_2^0)=0,\quad \mathrm{b}_2^0(C^2+1)+(\mathrm{b}_0^0-\mathrm{b}_2^0)=0,\quad C((\mathrm{c}_3^0(C^2+1)+\mathrm{c}_1)=0, \tag{5.13}$$

where

$$\mathrm{a}_2^0=A^2(\Lambda+m_1A^2+m_3B^2)^2-\epsilon^2;\ \mathrm{b}_2^0=B^2(\Lambda+m_1B^2+m_3A^2)^2-\delta^2\epsilon^2,$$
$$\mathrm{a}_0^0=A^2(\Lambda+m_1A^2+m_2B^2)^2-\epsilon^2;\ \mathrm{b}_0^0=B^2(\Lambda+m_1B^2+m_2A^2)^2-\delta^2\epsilon^2,$$
$$\mathrm{c}_3^0=(\Lambda+m_1A^2+m_3B^2)\,(\Lambda+m_1B^2+m_3A^2).$$

The third equation of (5.13) yields the alternative: *either* $C=0$ *or* $c_3(C^2+1)+c_1=0$. Because of the standing wave criterion (5.9), the first case implies a *standing* wave, but the second case corresponds to *swirling*.

Inserting $C=0$ into (5.13) reduces them to the equality $\mathrm{a}_0^0=\mathrm{b}_0^0=0$, which has the analytical solution

$$B^2\left((m_1-m_2)(B^2-A^2)\pm\epsilon/A\right)^2=\delta^2\epsilon^2,\quad \Lambda=\pm\,\epsilon/A-m_1A^2-m_2B^2. \tag{5.14}$$

The analytical solution suggests solving the first (cubic) equation (from one to three

positive roots $B^2 > 0$) for a given $\pm A$ and, thereafter, computing Λ for these $\pm A$ and B (the second equation).

When $C \neq 0$, substituting $(C^2+1) = -c_1/c_3 > 1$ into the two first equations of (5.13) derives the system

$$\begin{cases} (\Lambda + m_1A^2 + m_3B^2)D(\Lambda; A, B) = (m_2 - m_3)\epsilon^2, \\ (\Lambda + m_1B^2 + m_3A^2)D(\Lambda; A, B) = (m_2 - m_3)\delta^2\epsilon^2, \\ 0 < (\Lambda + m_1A^2 + m_3B^2)(\Lambda + m_1B^2 + m_3A^2) \leqslant (m_3 - m_2)^2A^2B^2, \end{cases} \tag{5.15}$$

where the function

$$D(\Lambda; A^2, B^2) = 2\Lambda^2 + \Lambda(A^2 + B^2)(2m_1 + m_2 + m_3) + m_1(m_2 + m_3)(A^4 + B^4) + 2(m_1^2 + m_2m_3)A^2B^2 \tag{5.16}$$

commutates by variables A^2 and B^2. Structure of (5.15) requires

$$\Lambda(1 - \delta^2) + (m_3 - \delta^2m_1)A^2 + (m_1 - \delta^2m_3)B^2 = 0, \tag{5.17}$$

which, because $(m_3 - \delta^2m_1) > 0$ for $0.5 \lesssim h/L$ (figure 3), makes it possible to express A^2 as a linear combination of B^2 and Λ. Substituting this expression into the first/second equation of (5.15) derives a cubic equation with respect to B^2 whose coefficients are functions of Λ. This means that, for any fixed Λ, we can find the real positive roots B^2 as functions of Λ, but (5.17) returns the corresponding A^2. One can say that we have an analytical solution for $C \neq 0$.

The undamped steady-state resonant sloshing due to an oblique harmonic excitation with $0 < \delta < 1$ ($0 < \gamma < \pi/4$) can theoretically lead to maximum *six different standing* steady-state resonant *waves* (three for A and three for $-A$ by (5.14)). Each point on the corresponding response curves in the $(\sigma/\sigma_1, A, B)$ space determines a single steady-state wave from these six solutions. In the contrast, Part 1 reports three standing waves for longitudinal and diagonal harmonic excitations, which consist of one planar and two squares-likes resonant waves so that any point on the squares-like response curves corresponds to two physically-identical Stokes waves occurring with an angle to the excitation plane.

Equations (5.15) and $(C^2 + 1) = -c_1/c_3 \geqslant 1$ determine maximum *three physically-different undamped swirling* waves. Each point on the corresponding curves implies two physically-identical swirling waves (clock- and counterclockwise) associated with (Λ, A, B, C) and $(\Lambda, A, B, -C)$. By analysing [3] ($AB^2\mathcal{D}(\alpha) = \epsilon \sin\psi$) and [4] ($A^2B\mathcal{D}(\alpha) = \delta\epsilon \sin\varphi$), we derive these two waves as $z = S(x, y; A\cos\psi, B\cos\varphi)\cos\bar{\sigma}t + S(x, y; A\sin|\psi|, B\sin|\varphi|)\sin\bar{\sigma}t + o(\epsilon^{1/3})$ and $z = S(x, y; A\cos\psi, B\cos\varphi)\cos\bar{\sigma}t - S(x, y; A\sin|\psi|, B\sin|\varphi|)\sin\bar{\sigma}t + o(\epsilon^{1/3})$. The results for the undamped swirling are consistent with Part 1 where only longitudinal and diagonal harmonic excitations were considered.

5.3. *Damped steady-state resonant sloshing*

Except for the longitudinal forcing, we do not know how to construct an analytical solution of the secular equations for the damped sloshing with $O(\epsilon^{2/3}) = \xi > 0$. However, one can classify the corresponding steady-state solutions by using the standing wave criterion (5.9). When $A, B \geqslant 0$ and $\xi > 0$ in equations [3] and [4], the criterion leads to

$$\psi = \varphi + 2\pi i, \ i \in \mathbb{Z} \ \text{ and } \ B = \delta A. \tag{5.18}$$

5.3.1. *Longitudinal forcing*

When $\delta = 0$ and $\xi > 0$, (5.7) transforms (5.2a) to the form (5.6), which we rewrite as

$$\begin{cases} A^2\left(\xi^2 + [\Lambda + m_1 A^2]^2\right) = \epsilon^2, \\ 0 < A \leqslant \epsilon/\xi;\ B = 0;\ 0 \leqslant \psi = \varphi = \arccos A\,[\Lambda + m_1 A^2]/\epsilon \leqslant \pi. \end{cases} \tag{5.19}$$

The roots describe the *planar* steady-state standing wave by the first Stokes mode

$$z = A\cos(\bar{\sigma}t - \psi)\, f_1^{(1)}(x) + o(\epsilon^{1/3}). \tag{5.20}$$

The squares-like standing waves are impossible for the damped sloshing.

To describe swirling, we rewrite (5.8) in the form

$$\begin{cases} A\left[\Lambda + m_1 A^2 + \dfrac{m_2 + m_3\, C^2}{1 + C^2} B^2\right] = \epsilon\cos\psi;\ A\left[\dfrac{(m_3 - m_2)C}{1 + C^2} B^2 + \xi\right] = \epsilon\sin\psi; \\ B^2 = -\dfrac{1}{m_1}\left[\Lambda + \dfrac{m_2 + m_3\, C^2}{1 + C^2} A^2\right] > 0;\ A^2 = \dfrac{\xi\,(1 + C^2)}{(m_3 - m_2)\, C} > 0. \end{cases} \tag{5.21}$$

Consequently substituting expressions for A^2 and B^2 into the square sum of the first row equations gives the nonlinear algebraic equation with respect to C:

$$q_6 C^6 + q_5 C^5 + q_4 C^4 + q_3 C^3 + q_2 C^2 + q_1 C + q_0 = 0, \tag{5.22}$$

where

$$\begin{aligned} q_6 &= \xi^3 (m_1^2 - m_3^2)^2 > 0, \\ q_5 &= 2\xi^2 \Lambda\,(m_3 - m_2)(m_3 + m_1)(m_1 - m_3)^2, \\ q_4 &= \xi\left[\xi^2[3m_1^4 + (m_2^2 - 6m_2 m_3 - m_3^2)m_1^2 - 2m_1 m_3 (m_2 - m_3)^2 + m_2 m_3^2 (m_2 + 2m_3)]\right. \\ &\quad \left. + \Lambda^2 (m_2 - m_3)^2 (m_1 - m_3)^2\right], \\ q_3 &= \epsilon^2 (m_2 - m_3)^3 m_1^2 + 2\Lambda\xi^2\left[m_1 (m_2^3 - m_2^2 m_3 + m_2 m_3^2 - m_3^3)\right. \\ &\quad \left. + (m_2 - m_3)(m_1^2 (m_2 + m_3 - 2m_1) - m_2 m_3 (m_2 + m_3))\right], \\ q_2 &= \xi\left[\Lambda^2 (m_2 - m_3)^2 (m_1 - m_2)^2\right. \\ &\quad \left. + \xi^2 [3m_1^4 + (-m_2^2 - 6m_2 m_3 + m_3^2)m_1^2 - 2m_1 m_2 (m_2 - m_3)^2 + m_2^2 m_3 (2m_2 + m_3)]\right], \\ q_1 &= 2\xi^2 \Lambda\,(m_3 - m_2)(m_1 + m_2)(m_1 - m_2)^2, \\ q_0 &= \xi^3 (m_1^2 - m_2^2)^2 > 0 \end{aligned}$$

are functions of Λ. The polynomial equation (5.22) has maximum six positive roots C ($(m_3 - m_2) > 0$ in the last formula of (5.21)). Substituting these roots in expressions for A^2 and B^2 of (5.21) computes $(\sigma/\sigma_1, A, B, C)$, which implies a point on the corresponding response curves. Because $\delta = 0$, a unique phase-lag φ cannot be found; φ are restored for each $C = \tan\alpha$ as $\varphi_1 = \psi + \alpha$ and $\varphi_2 = \psi + \alpha \pm \pi$. Physically, these two phase-lags $\varphi_{1,2}$ for each point $(\sigma/\sigma_1, A, B, C)$ on the response curves mean that the point determines two physically-identical swirling waves (clockwise and counterclockwise).

5.3.2. *Diagonal forcing*

When $\delta = 1$, (5.18) transforms (5.2a) to the form

$$\begin{cases} A^2\left(\xi^2 + [\Lambda + (m_1 + m_2)A^2]^2\right) = \epsilon^2, \\ A = B > 0,\quad 0 \leqslant \psi = \varphi = \arccos A\,[\Lambda + (m_1 + m_2)A^2]/\epsilon \leqslant \pi, \end{cases} \tag{5.23}$$

whose solution describes the *diagonal* wave

$$z = A\cos(\bar{\sigma}t - \psi)\, S(x, y; 1, 1) + o(\epsilon^{1/3}) \tag{5.24}$$

by the combined diagonal-type Stokes mode $S(x, y; 1, 1)$. *The squares-like standing waves are impossible* for the diagonally-forced damped sloshing.

The diagonally-forced undamped sloshing requires $A = B$ (the wave amplitudes are equal in the Ox and Oy directions). This fact was extensively discussed in Part 1. Substituting $A = B$ in $\boxed{1}$ and $\boxed{2}$ of (5.2a) for the damped sloshing ($\xi > 0$) leads to either $\varphi = \psi$ (corresponds to the diagonal wave) or $\varphi = -\psi$. The latter condition means that the left-hand sides of $\boxed{3}$ and $\boxed{4}$ are equal and, therefore, $2A\xi = 2B\xi = (A+B)\xi = 0$, which is impossible. As a consequence, the diagonally-forced swirling is characterised by the non-equal wave responses along the perpendicular walls.

5.3.3. *Oblique forcing*

When $0 < \delta < 1$, substituting the standing wave criterion (5.18) into (5.2) and taking the difference of $\boxed{1}$ and $\boxed{2}$ derive $(m_1 - m_2)(1-\delta^2)A^3 = 0$. Figure 3 shows that $m_1 > m_2$ and, therefore, this equality is never fulfilled. As a consequence, the *standing* resonant wave regime is *not* possible for the oblique non-diagonal forcing with $0 < \delta < 1$. *All steady-state resonant waves are formally of the swirling type.*

5.3.4. *Summary*

Theoretical results on the *damped resonant sloshing* in sections 5.3.1–5.3.3 show that (A) the standing resonant waves exist *only* for longitudinal and diagonal harmonic excitations, these are of planar or diagonal types, respectively, (B) the squares-like standing waves are impossible, (C) for the oblique non-diagonal forcing with $0 < \delta < 0$, all the damped steady-state sloshing regimes are of the swirling type, (D) when asymptotic condition (5.12) (the nonzero C is relatively small) is satisfied, the corresponding swirling becomes close to a standing wave by a modified Stokes mode so that it can be treated as an *almost-standing* wave, (E) two physically-identical swirling waves of the opposite angular directions are only possible for the longitudinal forcing, (F) for the oblique forcing with $\gamma \neq 0$, each point on the response curves implies a unique swirling wave whose amplitudes along Ox and Oy axes are never equal, even for the diagonal forcing.

6. Damped versus undamped response curves

The undamped response curves for the *longitudinal* forcing ($\delta = \gamma = 0$) were extensively analysed and discussed in Part 1 for various liquid depths and forcing amplitudes. Figure 4 (a) shows the corresponding response curves in terms of the 'integral' amplitudes A and B, which present the dominant sin- and cos-components in a_1 and b_1. To get A and B, we use, in fact, an exact asymptotic solution of the modal system constructed in Appendix A. The solution neglects the $o(\epsilon)$-quantities but the modal equations (2.5)-(2.6) are also derived within to the $O(\epsilon)$-order sloshing component.

In our numerical analysis, we will present a three-dimensional view in the $(\sigma/\sigma_1, A, B)$ space and its projections on the $(\sigma/\sigma_1, A)$ and $(\sigma/\sigma_1, B)$ planes. The panel (b) of the figure depicts the corresponding response curves for the *damped* sloshing ($\xi = 0.0256$). The solid lines specify stable solutions. The computations were done with the nondimensional forcing amplitude $\eta = \eta_{1a} = 0.0075\,(\eta_{2a} = 0)$ and $h/L = 0.6$. Because m_1, m_2 and m_3 weakly depend on h/L for $0.5 \lesssim h/L$, the branching should be similar for these relatively-high liquid depth-to-tank breadth ratios. The latter fact

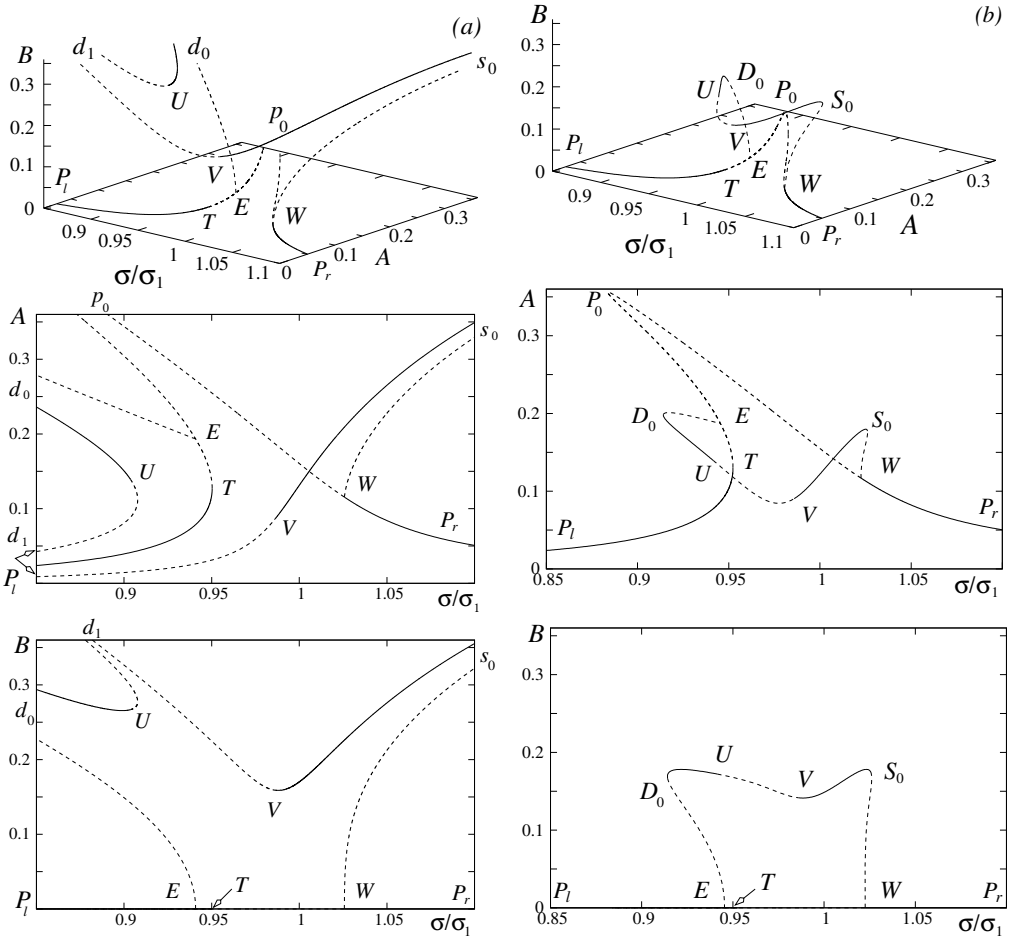

FIGURE 4. The steady-state waves response curves in the $(\sigma/\sigma_1, A, B)$ space and their projection on the $(\sigma/\sigma_1, A)$ and $(\sigma/\sigma_1, B)$ planes for the undamped (panel a) and damped (panel b) cases. The longitudinal forcing with the nondimensional amplitude $\eta = \eta_{1a} = 0.0075$ and $h/L = 0.6$. The solid lines specify stable solutions. The branches $P_lTEP_0(p_0)$ and $P_rWP_0(p_0)$ belong to the $(\sigma/\sigma_1, A)$ plane. They correspond to the planar standing waves. The small letters p_0, d_0, d_1 and s_0 in (a) mean that the corresponding branches meet at the infinity. The squares-like standing waves exist for the undamped case (b). They are presented by the two branches d_1Ud_0 and d_0E. The undamped swirling corresponds to Ws_0Vd_1. The squares-like waves disappears in the damped case (b). The branch ED_0UVS_0W represents in panel (b) a swirling wave mode. However, computations show that condition (5.12) is satisfied on the stable sloshing subbranch D_0U and, therefore, the subbranch represents an almost standing wave by a modified Stokes mode (close to a square-like wave in the panel a). All steady-state waves are unstable in the frequency range between T and V where irregular (chaotic) wave motions are expected. Results in (a) are based on computation schemes from Part 1. Computational formulas for getting (b) are presented in section 5.3.1.

is also true for figures 5–8 where we present the response curves for the oblique forcing with $\gamma = \pi/36 = 5^0, \pi/6 = 30^0, \pi/4.5 = 40^0$ and $\pi/4 = 45^0$, respectively. *Henceforth*, the small letters (p_0, d_0, s_0 and d_1) are used to specify the fact that the corresponding branches meet at the infinity.

The undamped planar sloshing corresponds to $B = 0$, $C = 0$, $\xi = 0$ and $A > 0$ in (5.7) so that the non-zero amplitude A is then governed by the cubic equation $A(\Lambda + m_1A^2) = \epsilon$

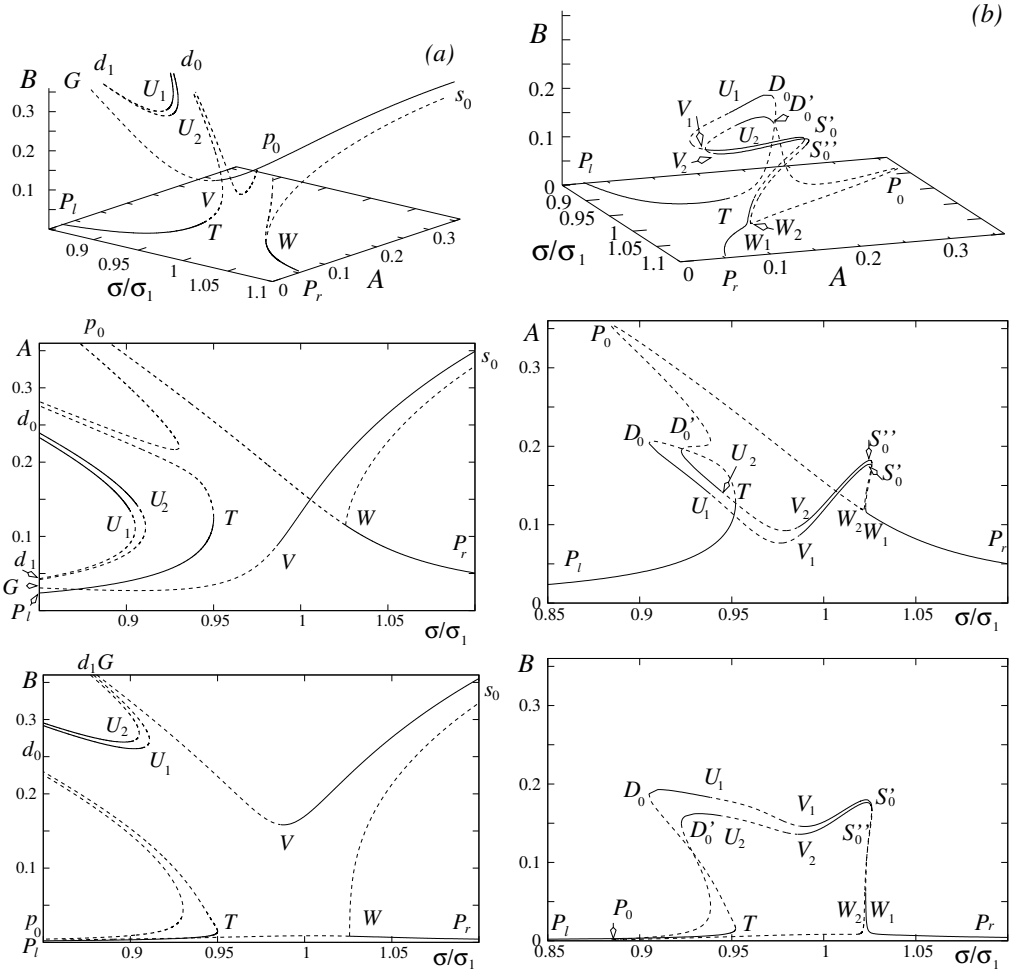

FIGURE 5. Similar to figure 4 but for an oblique forcing with $\gamma = 5^0 = \pi/36$. The non-zero γ splits the connected branch $P_lT(E)p_0(P_0)$ in figure 4 at the bifurcation point E. The undamped *case (a)* is characterised by five categories of standing resonant waves (maximum six are possible possible according to the theory). They are represented by the branches P_lTd_0, d_0p_0, d_1U1d_0, $d_1U_2d_0$ and P_rWp_0. Each point on these branches implies a single standing wave type (not two as in figure 4 for the squares-like wave mode). Because γ is relatively small, the stable subbranches P_lT and P_rW correspond to the nearly-planar standing waves. The swirling-related branches are Ws_0 and s_0VG where G belongs to $d_1U_1d_0$ (has coordinates $(\sigma/\sigma_1, A, B) = (0.83, 0.04, 0.4)$ in this numerical example). In the *panel (b)*, the nonzero damping and angle γ split the response curves at both E and W from figure 4. There appear two non-connected branches $P_lTD_0U_1V_1S_0'W_1P_r$ and (loop-like) $P_0D_0'U_2V_2S_0''W_2P_0$. Formally, each point on these branches imply a single (stable/unstable) swirling wave. Computations show that (5.12) is satisfied on the stable subbranches P_lT and P_rW_1 (almost planar wave) as well as on U_1D_0 and U_2D_0'. The point G in the panel (a) coincides with $U_1$for the damped case (b). Results in (a) are based on formulas (5.14) (standing waves) and (5.15) (swirling). Results for (b) are a numerical solution of (5.11) (computational details are given in Supplementary Materials).

(see, condition (5.9) and equations (5.3), (5.6) with $\delta = \xi = 0$). The phase-lags are $\psi = 0$ for $(\Lambda + m_1A^2) > 0$ and $\psi = \pi$ as $(\Lambda + m_1A^2) < 0$. The second phase-lag φ is associated with the zero cross-wave component ($B = 0$) and, therefore, it has no a physical meaning. Because the standing wave condition (5.9) requires $\sin(\varphi - \psi) = 0$, one can take $\varphi = \psi$.

The undamped planar steady-state waves are represented by the branches P_lTEp_0 and P_rWp_0 in figure 4 (a). The branches belong to the $(\sigma/\sigma_1, A)$ plane. They are invisible (coincide with the horizontal axis) in projection on the $(\sigma/\sigma_1, B)$ plane. An extensive discussion of the turning point T and the bifurcation points E and W can be found in Part 1. The bifurcation points E and W are origins of the squares-like and swirling waves, respectively. The planar resonant waves are stable for the forcing frequencies in the left of T and in the right of W.

Setting $\xi = 0$ in (5.8) makes it possible to consider the three-dimensional undamped steady-state sloshing with $B \neq 0$ due to the longitudinal forcing. The last equation of (5.8) deduces that $\mathcal{D}(\alpha) = 0$ and, thereby, we arrive at the alternative: either $\sin\alpha = 0$ or $\cos\alpha = 0$. Because of (5.9), the first case ($\sin\alpha = 0$) implies three-dimensional (non-planar) standing waves, which are, as we know from Part 1, the *square-like* resonant steady-state sloshing. When $\cos\alpha = \cos(\varphi - \psi) = 0$, the secular equations (5.8) with $\xi = 0$ govern the undamped *swirling*.

Substituting $\sin\alpha = 0$ in (5.8) derives $A^2(\Lambda + m_1A^2 + m_2B^2)^2 = \epsilon^2$ and $(\Lambda + m_1B^2 + m_2A^2) = 0$, which govern the nondimensional amplitudes A and B of the squares-like wave regime. The phase-lag $\psi = 0$ for $(\Lambda + m_1A^2 + m_2B^2) > 0$ and $\psi = \pi$ when $(\Lambda + m_1A^2 + m_2B^2) < 0$. Another phase-lag φ follows from the standing wave condition (5.9), $\sin(\varphi - \psi) = 0$. It equals to either $\varphi = \psi$ or $= \psi \pm \pi$. The non-uniqueness of φ implies *two* different squares-like waves for each point of the corresponding response curves in the $(\sigma/\sigma_1, A, B)$ space. These two squares-like standing waves are defined by $z = \pm S(x, y; A, B)\cos\bar{\sigma}t + o(\epsilon^{1/3})$ and $z = \pm S(x, y; A, -B)\cos\bar{\sigma}t + o(\epsilon^{1/3})$. They can be treated as occurring with an equal (positive and negative) angle relative to the forcing plane Oxz. The squares-like sloshing is presented in figure 4 (a) by the two branches Ed_0 and d_1Ud_0. The (unstable waves) branch Ed_0 emerges from the bifurcation point E. Point U divides d_1Ud_0 into Ud_0 (stable squares-like sloshing) and Ud_1 (unstable one).

In the second case ($\cos\alpha = \cos(\varphi - \psi) = 0$, undamped swirling), amplitudes A and B are computed from $A^2(\Lambda + m_1A^2 + m_3B^2)^2 = \epsilon^2$ and $(\Lambda + m_1B^2 + m_3A^2) = 0$. The first phase-lag $\psi = 0$ for $(\Lambda + m_1A^2 + m_3B^2) > 0$ and $\psi = \pi$ when $(\Lambda + m_1A^2 + m_3B^2) < 0$. Because $\delta = 0$, the second phase-lag φ cannot be directly computed by using (5.2*a*). Requiring $\cos\alpha = 0$ deduces however that $\varphi = \psi \pm \pi/2$. Accounting for (4.2) and (5.1*b*), $\pm\pi/2$ for φ implies two swirling waves for each point on the corresponding branches in the $(\sigma/\sigma_1, A, B)$ space. These two waves are $z = \pm(Af_1^{(1)}(x)\cos\bar{\sigma}t + Bf_1^{(2)}(y)\sin\bar{\sigma}t) + o(\epsilon^{1/3})$ and $z = \pm(Af_1^{(1)}(x)\cos\bar{\sigma}t - Bf_1^{(2)}(y)\sin\bar{\sigma}t) + o(\epsilon^{1/3})$. They are physically identical and only differ by the propagating angle direction, clockwise or counterclockwise. The undamped swirling regime is represented by the branches Ws_0 and d_1Vs_0 in figure 4 (a). The (unstable swirling) branch Ws_0 emerges from the planar-wave response curves at the bifurcation point W. Another swirling-related branch d_1Vs_0 is divided by V into stable and unstable subbranches.

For the undamped longitudinally-forced sloshing, irregular (chaotic) waves are possible for the forcing frequencies laying between the abscissas of T and V. This fact was extensively discussed in Part 1.

The response curves for the *damped* steady-state sloshing due to the *longitudinal* forcing are drawn by using the analytical solution (5.19)–(5.22). Figure 4 (b) illustrates the numerical output for $\xi = 0.0256$. According to our results from section 5.3.1, the damped squares-like waves are impossible. The connected branch $P_lTEP_0WP_r$ belongs to the $(\sigma/\sigma_1, A)$-plane; it is responsible for the planar waves (P_0 is not at the infinity). The damping saves the two bifurcation points E and W. These points are now two origins for the damped swirling, which is represented by the arc-like branch ED_0UVS_0W. The

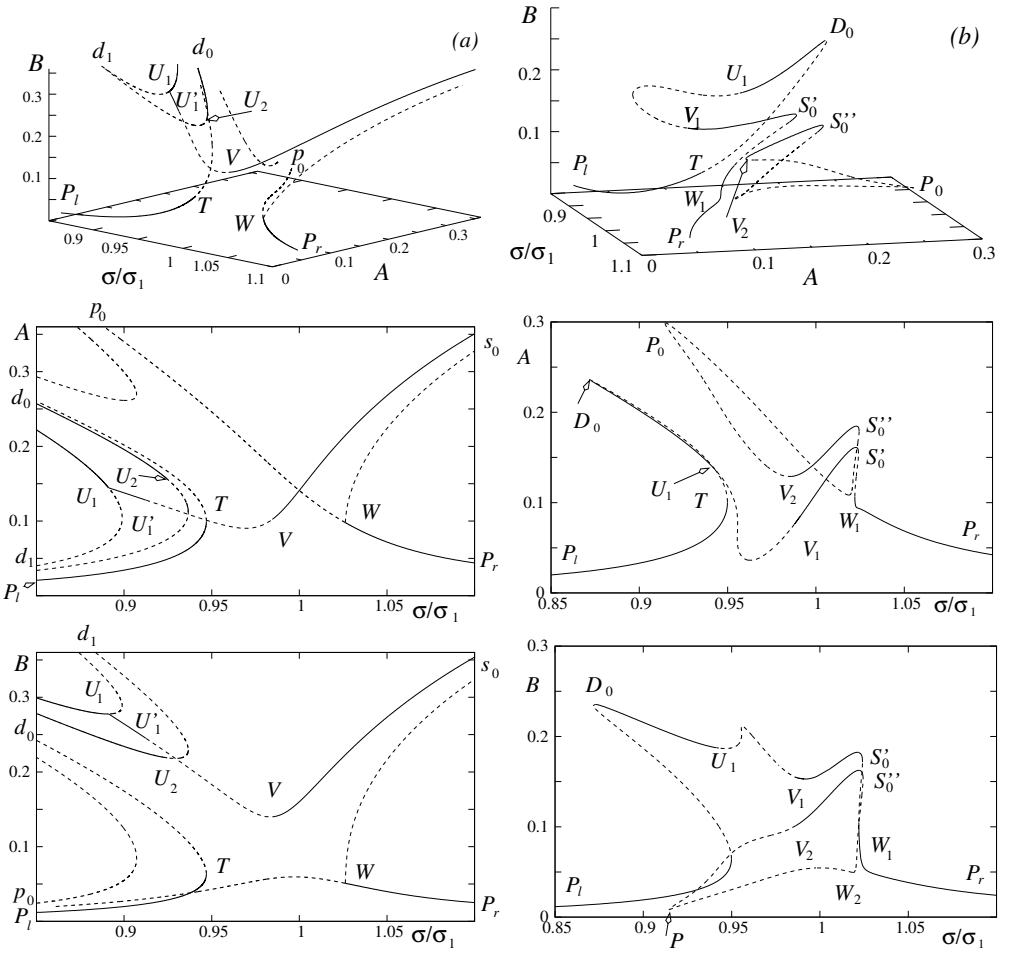

FIGURE 6. The same as in figure 5 but for $\gamma = 30^0$. A novelty in the panel (a) [undamped sloshing] is that an extra stable swirling subbranch U_1U_1' appears with increasing γ. The damped sloshing response curves in the panel (b) show vanishing the stable almost standing waves (U_1D_0' in figure 5 b). The loop-like branch $P_0W_1S_0''V_2P_0$ has now only one stable piece V_2S_0'' corresponding to swirling (condition (5.12) is not satisfied). Results in (a) are based on formulas (5.14) (standing waves) and (5.15) (swirling). Results for (b) are a numerical solution of (5.11) (computational details are given in Supplementary Materials).

points D_0 and S_0 are not at the infinity now; d_1 disappears. Computations show that the asymptotic condition (5.12) is satisfied on the (stable sloshing) subbranch D_0U. This means that the subbranch represents an almost standing wave when a modified Stokes mode dominates. This mode is close to a squares-like wave on Ud_0 in the panel (a). The linear damping ratio $\xi = 0.0256$ gives a negligible effect on positions of V and T. As a consequence, the frequency range, where irregular waves are expected, remain almost the same in (a) and (b).

One should note that Ikeda *et al.* (2012) numerically detected both irregular and regular (periodic) damped sloshing between T and V by using their adaptive multimodal system with linear damping terms. A dedicated model tests are needed to quantify whether the regular sloshing exists in this frequency range and, thereby, clarify whether

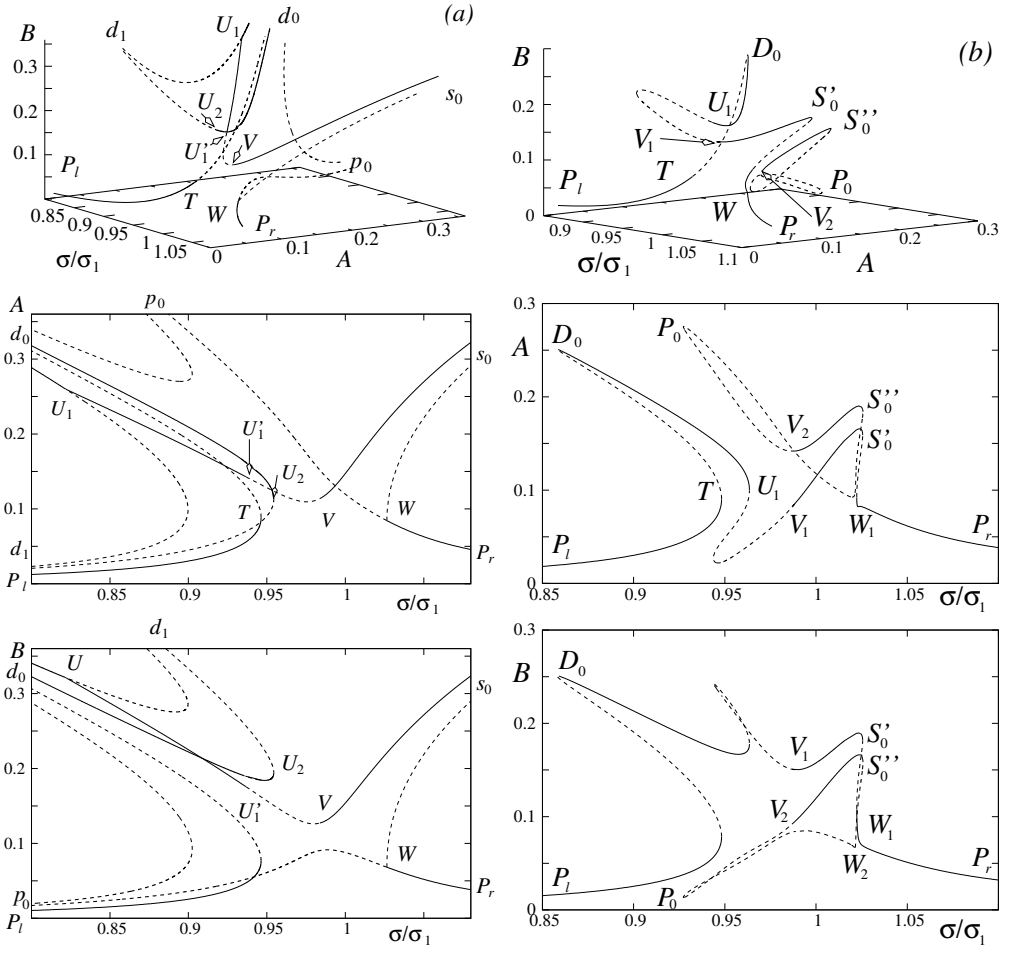

FIGURE 7. The same as in figure 6 but for $\gamma = 40^0$. For the undamped case in (a), the subbranches $d_0U_1U_1'Vs_0$, Ws_0 and U_2d_0 tend the $A = B$ plane. The first two subbranches convert to the undamped swirling but U_2d_0 should turn into the diagonal standing wave (the limit is shown in figure 8 a). In the panel (b), the swirling-related response curves do not belong to the $A = B$ plane as $\gamma \to \pi/4$. As a consequence, only U_1D_0 tends to the plane. It convert to the diagonal standing wave for $\gamma = \pi/4$. Results in (a) are based on formulas (5.14) (standing waves) and (5.15) (swirling). Results for (b) are a numerical solution of (5.11) (computational details are given in Supplementary Materials).

one should switch to an adaptive asymptotic ordering from the Narimanov–Moiseev one for a better description of the resonant sloshing in this frequency range.

Almost longitudinal forcing ($\gamma = \pi/36 = 5^0$) is considered in figure 5. When comparing the undamped sloshing in panels (a) of figures 4 and 5, one should remember that the oblique forcing admits up to six different standing waves. We identify five categories of those standing waves represented by the branches P_lTd_0, d_0p_0, d_1U1d_0, $d_1U_2d_0$ and P_rWp_0. The former d_1Ud_0 in figure 4 (a) splits into the two branches $d_1U_1d_0$ and $d_1U_2d_0$, but the bifurcation point E vanishes so that the former P_lTEp_0 is divided into P_lTd_0 and d_0p_0. In contrast to the longitudinal forcing in figure 4 (a), each point on the branches implies only one unique standing wave. Two pieces of P_rWp_0 and P_lTd_0 are close to the horizontal plane $B = 0$; they imply an almost planar stable steady-state wave regime.

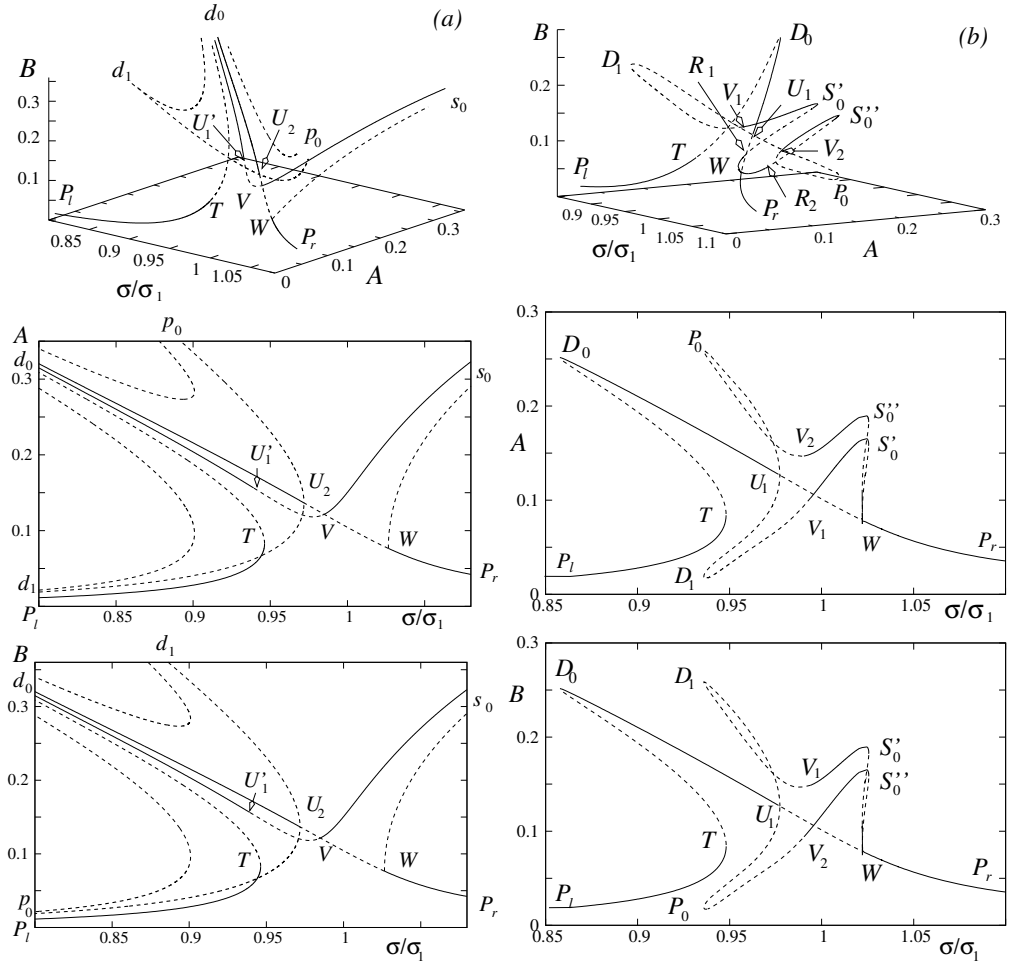

FIGURE 8. The same as in figure 6 but for the diagonal forcing with $\gamma = 45^0 = \pi/4$. In the panel (a), all branches away from the $A = B$ plane correspond to the squares-like standing wave regime; U_2 is the corresponding bifurcation point for this regime. The branches $P_l T d_0$, $P_r W$ and $U_2 d_0$ imply the diagonal standing waves. The branches $d_0 U_1' V s_0$ and $W s_0$ correspond to swirling (two physically-identical waves in clockwise and counterclockwise directions, respectively). Only diagonal standing waves belong to the $A = B$ plane in the damped case (b): the branch $P_l T D_0 W P_r$. The (stable sloshing) subbranches WR_1, WR_2, $S_0' V_1$ and $S_0'' V_2$ correspond to swirling (condition (5.12) is not satisfied on them). Results in (a) are based on formulas (5.14) (standing waves) and (5.15) (swirling). Results for (b) are a numerical solution of (5.11) (computational details are given in Supplementary Materials).

Other points on the aforementioned five branches correspond to a squares-like standing wave. The swirling wave regime is represented by $W s_0$ and $s_0 V G$. A novelty is that the latter branch meets $d_1 U_1 d_0$ at a point G (coordinates $(\sigma/\sigma_1, A, B) = (0.83, 0.04, 0.4)$ in this numerical example). Each point on the swirling-related branches corresponds to two identical (clockwise and counterclockwise) swirling waves.

A complex effect of the non-zero γ and damping on the response curves is demonstrated in figure 5 (b). The branching should be compared with that in figure 4 (b) as well as with the panel (a). We see that $\xi = O(\epsilon^{2/3})$ and a relatively-small γ split the response curves at both E and W from figure 4. As a consequence, the two non-connected branches

$P_lTD_0U_1V_1S_0'W_1P_r$ and (loop-like) $P_0D_0'U_2V_2S_0''W_2P_0$ appear. Both of them have very attractive geometry, especially, in the $(\sigma/\sigma_1, A, B)$ space. Each point on these response curves implies swirling. However, computations show that (5.12) is satisfied on the stable subbranches P_lT and P_rW_1 (almost planar wave) as well as on U_1D_0 and U_2D_0'. The point G from the panel (a) coincides with U_1 for the damped case. The most important effect of the non-zero γ for an oblique forcing is that the two physically-identical swirling waves (clockwise and counterclockwise) split into two different ones. We can see this effect by comparing the panels (a) and (b) in figure 5. Condition (5.12) is satisfied on V_1S_0' and V_2S_0'' and, therefore, two swirling waves of different amplitudes along the Ox and Oy axes are expected represented by these stable sloshing subbranches.

Figures 6 and 7 demonstrate what happens with the response curves with a further increase of γ. The trends are different for the damped and undamped cases. The panels (a) show that, after G met U_1, an extra subbranch U_1U_1' appears, which implies a stable swirling. With increasing γ close to $\pi/4$, U_1 moves away from the primary resonance zone, but $U_1U_1'Vs_0$ tends laying in the $A = B$ plane. The latter will be responsible for the diagonally-exited swirling in figure 8. Another subbranch U_2d_0 also approaches the $A = B$ plane; it corresponds to the diagonal wave as $\gamma = \pi/4$. The damped sloshing response curves in the panels (b) of figures 6 and 7 show that the linear damping erases the U_2D_0' subbranch for non-small γ. They also confirm that the plane $A = B$ contains only response curves of the diagonal wave regime.

The diagonal wave regime for $\gamma = \pi/4$ (diagonal forcing) is characterised by three stable sloshing subbranches. They must belong to the $A = B$ plane. Figure 8 shows the latter fact for both damped and undamped sloshing. The subbranches P_lT and P_rW transform from the stable planar waves as γ changes from 0 to $\pi/4$. Part 1 describes another stable diagonal sloshing subbranch, which should be situated over P_lT. Considering the limit $\gamma \to \pi/4$ shows that the third subbranch results from the stable standing wave regimes on U_2d_0 but, because the linear damping annihilates U_2D_0', the stable diagonal waves are represented by U_1D_0.

7. Comparison with experiments

Ikeda *et al.* (2012) conducted relevant experimental studies on the steady-state wave regimes for the damped liquid sloshing. The maximum wave elevations near the two perpendicular walls (at the points $(x_0\,L, 0)$ and $(0, x_0\,L)$ with $x_0 = 0.4$) were measured including for standing, swirling and irregular wave motions. The experimental data are reported for the longitudinal ($\gamma = 0$), oblique ($\gamma = \pi/6$) and diagonal ($\gamma = \pi/4$) cases. The forcing amplitudes are slightly different and equal to $\eta = 0.00727$, 0.00726, and 0.00717, respectively. In the model tests, the liquid depth ratio is $h/L = 0.6$. Before presenting the experimental measurements, they extensively discussed in their Fig. 4, what kind of stable and unstable steady-state resonant waves are observed for these three experimental cases. This includes a discussion on the stable waves, which, normally, correspond to the standing (planar and diagonal) waves or what we called an almost standing waves (see, discussion around the asymptotic condition (5.12)). A special emphasis of Ikeda *et al.* (2012) was also placed on the fact that two swirling waves with the different angular directions are characterised by different maximum elevations at the measurement probes for the non-longitudinal forcing.

These experimental measurements of the L-scaled maximum steady-state wave elevations, $\zeta_x^{\max}$ and $\zeta_y^{\max}$, at the probes $(x_0\,L, 0)$ and $(0, x_0\,L)$ ($x_0 = 0.4$) are compared with our asymptotic modal prediction in figures 9–11. We computed these maximum wave

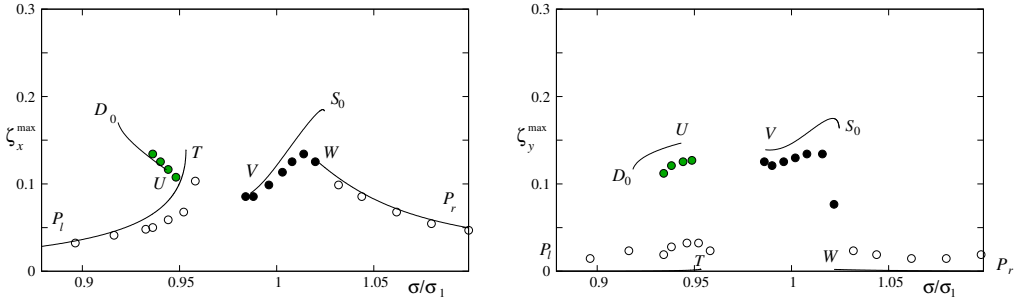

FIGURE 9. The experimental (Ikeda *et al.* 2012) and theoretical L-scaled maximum wave elevations at $(0.4\,L, 0)$ (marked by $\zeta_x^{\max}$) and $(0, 0.4\,L)$ ($\zeta_y^{\max}$) for the longitudinal forcing along the Ox axis. The nondimensional forcing amplitude is $\eta = \eta_{1a} = 0.00727$ ($\eta_{2a} = 0$) and the mean liquid depth is $h/L = 0.6$. The solid lines denote the computed maximum wave elevations for the stable steady-state regimes. The computations used $\xi = 0.0256$, which corresponds to the experimental logarithmic decrement estimated by Ikeda *et al.* (2012). The empty circles correspond to the experimental planar regime but the filled circles indicate swirling. The green/grey filled circles correspond in our classification to an almost standing wave in which one from two modified Stokes mode dominates (formally, it is a swirling mode). The theoretical subbranches adopted notations of the response curves in figure 4 (b).

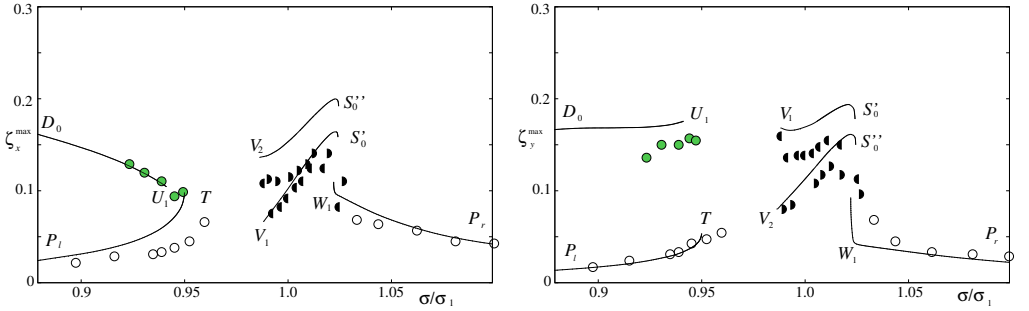

FIGURE 10. The same as in figure 9 but for $\gamma = \pi/6$. The half-circles denote the experimental swirling of the two different angular propagation directions that should theoretically belong, depending on the angular direction, to different branches, either $V_1 S_0'$ or $V_2 S_0''$. The response curves in terms of the lowest-order amplitude components A (Ox direction) and B (Oy for this experimental are presented in figure 6 (b).

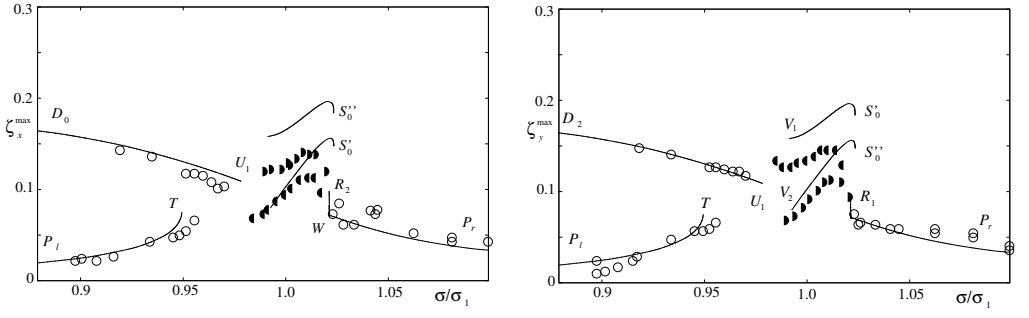

FIGURE 11. The same as in figure 10 but for $\gamma = \pi/4$ (the diagonal forcing). Only diagonal standing waves and swirling are possible. The experimental diagonal waves are marked by empty circles. The half-circles denote the two different experimental swirling modes of the different angular direction. The swirling modes are associated with the subbranches $V_1 S_0'$ and $V_2 S_0''$ in figure 8.

elevations as described in Appendix B. Readers can see that we accounted for actual positions of the measurement probes as well as contributions given by all nonlinearly-involved generalised coordinates, from $O(\eta^{1/3})$ to $O(\eta)$. The authors experience says that working with asymptotic nonlinear solutions of the resonant sloshing problems requires accounting for the higher-order contributions. Finally, we do not speculate with the damping coefficients but use $\xi = 0.0256$, which Ikeda *et al.* (2012) experimentally found by estimating the logarithmic decrements.

The theoretical stable steady-state wave elevations are marked in figures 9–11 by the solid lines. The experimental notation symbols are partly adopted from the corresponding figures by Ikeda *et al.* (2012). Empty circles mark the measured maximum wave elevations for standing waves (planar and diagonal), the green/grey filled circles appear in figures 9 and 10 to specify the almost standing waves. The half-circles (filled) are used to detect the two swirling modes of the different angular directions when these directions dictate non-equal maximum wave elevations at the perpendicular walls. The filled circles are used in figure 9 for the longitudinal forcing where the swirling direction was not important according to Ikeda *et al.* (2012) and our theoretical predictions.

Figure 9 presents the experimental and theoretical results for the longitudinal forcing along the Ox-axis. The theoretical subbranches adopt notations from figure 4. First, we note that the theoretical frequency ranges for the stable steady-state sloshing are generally good predicted, especially for the frequency zone between T (lower bound) and V (upper bound) where irregular waves are theoretically expected. This range was supported by the model tests. However, the theoretical points D_0 and S_0 are located rather far from the experimentally detected ones. Ikeda *et al.* (2012) increased ξ to 0.03 for a more precise theoretical prediction of these points. Our speculative numerical experiments showed this increase really helps for a better fit of these point positions. It also provides a better agreement for $\zeta_y^{\max}$ in the swirling case. One interesting point is a clearly non-zero experimental values of $\zeta_y^{\max}$ for the planar wave regime (P_lT and WP_r). Accounting for the second- and third-order generalised coordinates makes this elevation non-zero but the actual experimental values are clearly larger. We do not know how to explain this fact.

Figure 10 illustrates the theoretical and experimental maximum steady-state wave elevations for the oblique forcing with $\gamma = \pi/6$. The response curves in terms of the lowest-order amplitude components A (Ox direction) and B (Oy) for this experimental case are presented in figure 6 (b). The half-circles denote the experimental swirling modes of the two different angular directions that should theoretically belong to either V_1S_0' or V_2S_0'' of figure 6 (b). Again, we should remark on a problem in a precise prediction of the larger swirling amplitude of the two swirling modes for both $\zeta_x^{\max}$ and $\zeta_y^{\max}$, which can be fixed by a speculatively increase of the damping coefficient ξ from 0.0256 to 0.03. Because this happens for the larger wave elevations, this may be related to the dynamic contact angle damping, as Keulegan (1959) suggested. This kind of damping (Shukhmurzaev 1997) is of the nonlinear nature and, therefore, may increase with amplitudes.

Figure 11 focuses on the diagonal forcing with $\gamma = \pi/4$. A difference from figures 9 and 10 is the absence of the green/grey circles marking the almost standing wave regime. We expect only stable diagonal and swirling waves. The first one is well predicted, but, as it has been commented earlier, the asymptotic theory cannot well approximate the maximum wave elevation for the swirling modes.

One must note that Ikeda *et al.* (2012) performed their own computations. An adaptive multimodal theory was used. Their theoretical results may look better than our computations in some frequency ranges where swirling occurs but has a similar precision for other frequency ranges. We did not compare our asymptotic modal steady-state results with

their computations. The reasons for that are that, first, Ikeda *et al.* (2012) neglected the $O(\eta^{2/3})$ and $O(\eta)$ generalised coordinates when computing the elevations, which must, in our opinion, be included, secondly, they adopted a speculatively larger $\xi = 0.03$ for a better fit of the experimental measurements, thirdly, the authors most probably (we did not find out an answer in the text) did not account for the actual positions of the measurement probes. As we remarked above, after adopting the speculatively larger ξ, our results would possess a better accuracy for swirling.

8. Conclusions

A motivation for starting this study has been a series of qualitative differences between theoretical and experimental results, which we and some other authors obtained for the resonant sloshing in a square base tank, and experiments and computations by Ikeda *et al.* (2012). These were discussed in the Introduction and denoted as differences between (i)–(iii) and (i')–(iii'). After realising that these differences can be clarified by the linear damping effect, which may be rather important for relatively-small laboratory tanks, we found out a lack of knowledge on the undamped resonant sloshing (expected for large containers) when the forcing is neither longitudinal nor diagonal. This caused the threefold goal of the present paper. First, we generalise Part 1 for the oblique forcing. Second, we estimate when the linear damping can be important, establishing, in particular, that it really can matter for the laboratory tests by Ikeda *et al.* (2012) but can be neglected for our earlier experiments. Third, we mathematically explain the aforementioned differences as well as performed some computations to compare the response curves for the damped and undamped cases. All the results remain true for the liquid depth-to-tank width ratio $0.5 \lesssim h/L$ as we have discussed in the context of figure 3.

For the *undamped* resonant steady-state sloshing, we were able to find an analytical solution of the corresponding secular (necessary solvability condition) system for any oblique forcing. Based on this solution, one concludes that there are theoretically possible, for a given forcing frequency, maximum *six different standing* steady-state resonant *waves*. Each point on the corresponding response curves determines a single steady-state wave from these six solutions. On the contrary, Part 1 reports maximum three standing waves for longitudinal and diagonal harmonic excitations, which consist of one planar and two squares-likes resonant waves so that any point on the squares-like response curves corresponds to the two physically-identical Stokes waves occurring with an angle to the excitation plane. Each point on the undamped *swirling* response curves corresponds to physically-identical swirling waves (clock- and counterclockwise).

The main results on the *damped* resonant sloshing are: (A) the standing resonant waves exist only for longitudinal and diagonal harmonic excitations, these are of planar or diagonal types, respectively, (B) the squares-like standing waves are impossible, (C) for the oblique non-diagonal forcing with $0 < \delta < 0$, all the damped steady-state sloshing regimes are of the swirling type, (D) under the asymptotic condition (5.12), the damped swirling may become close to a standing wave by a modified Stokes mode so that the resonant sloshing can be treated as an *almost-standing* wave, (E) two physically-identical swirling waves of the opposite angular directions are only possible for the longitudinal forcing, (F) for the oblique forcing, each point on the response curves implies a swirling wave whose amplitudes along the Ox and Oy axes are never equal, even for the diagonal forcing. These results make it possible to explain the differences between (i)–(iii) and (i')–(iii') described in the Introduction. The results are extensively discussed by using the numerical response curves. The damped sloshing response curves are also compared

with those for the undamped ones. The latter comparison showed that a complex effect of the nonzero damping and angle γ between the forcing direction and the Ox-axis may significantly change both the branchings and the effective frequency ranges for swirling. Introducing the linear viscous damping is relevant for small-size laboratory tanks and very special applications exemplified by the packaging machines for the tetra-pack cardboard cartons.

We compared our results with the measured maximum wave elevations by Ikeda *et al.* (2012). A satisfactory agreement was found. The agreement for swirling can be improved by a speculative increase of the damping coefficient as Ikeda *et al.* (2012) has done. Because the maximum discrepancy happens for the larger swirling elevations, this increase can be qualitatively argued by nonlinear dynamic-contact angle damping (Shukhmurzaev 1997) and the strongly-nonlinear free-surface phenomena. In this context, the asymptotic linear damping ratio (3.3) makes it possible to evaluate only a lower bound for the total energy dissipation per a cycle. However, to the authors best knowledge, the literature does not give a method for quantifying the dynamic contact angle effect on the logarithmic decrements.

The authors acknowledge the financial support of the Centre of Autonomous Marine Operations and Systems (AMOS) whose main sponsor is the Norwegian Research Council (Project number 223254–AMOS).

Appendix A. The steady-state asymptotic solution of (2.5)-(2.6)

Following Faltinsen *et al.* (2003) and using (2.8), (3.2), we can derive an analytical solution of (2.5)-(2.6) in terms of $\epsilon^{1/3}$. The analytical procedure starts with the lowest-order approximation (4.1), which, being substituted into (2.5c)-(2.5e) gives

$$a_2 = p_0(a^2+\bar{a}^2) + h_0(a^2-\bar{a}^2)\cos 2\bar{\sigma}t + 2h_0 a\bar{a}\sin 2\bar{\sigma}t + o(\epsilon), \tag{A 1a}$$

$$b_2 = p_0(\bar{b}^2+b^2) + h_0(\bar{b}^2-b^2)\cos 2\bar{\sigma}t + 2h_0\bar{b}b\sin 2\bar{\sigma}t + o(\epsilon), \tag{A 1b}$$

$$c_1 = p_1(a\bar{b}+\bar{a}b) + h_1(a\bar{b}-\bar{a}b)\cos 2\bar{\sigma}t + h_1(\bar{a}\bar{b}+ab)\sin 2\bar{\sigma}t + o(\epsilon), \tag{A 1c}$$

where

$$p_0 = \frac{d_4-d_5}{2\bar{\sigma}_{2,0}^2};\quad h_0 = \frac{d_4+d_5}{2(\bar{\sigma}_{2,0}^2-4)};\quad p_1 = \frac{\hat{d}_1+\hat{d}_2-\hat{d}_3}{2\bar{\sigma}_{1,1}^2};\quad h_1 = \frac{\hat{d}_1+\hat{d}_2+\hat{d}_3}{2(\bar{\sigma}_{1,1}^2-4)}.$$

Owing to (2.8c) (no secondary resonance condition), coefficients p_0, h_0, p_1 and h_1 are formally of the order $O(1)$.

Furthermore, inserting (4.1) and (A 1) into (2.5a) and (2.5b) and gathering the first Fourier harmonic derive the solvability (secularity) equations (4.3) with respect to the unknown amplitude parameters $a, \bar{a}, b$ and $\bar{b}$. After finding $a, \bar{a}, b$ and $\bar{b}$ from (4.3) and gathering the super-harmonics in (2.5a) and (2.5b), we get

$$a_1 = a\cos\bar{\sigma}t + \bar{a}\sin\bar{\sigma}t + \big\{[a(n_1(-a^2+3\bar{a}^2)+n_2(b^2-\bar{b}^2)) + 2n_2 b\bar{a}\bar{b}]\cos 3\bar{\sigma}t$$
$$+[\bar{a}(n_1(\bar{a}^2-3a^2)+n_2(b^2-\bar{b}^2)) - 2n_2 ab\bar{b}]\sin 3\bar{\sigma}t\big\}/(9-\bar{\sigma}_{1,0}^2) + o(\epsilon), \tag{A 2}$$

$$b_1 = \bar{b}\cos\bar{\sigma}t + b\sin\bar{\sigma}t + \big\{[\bar{b}(n_1(-\bar{b}^2+3b^2)+n_2(\bar{a}^2-a^2)) + 2n_2 ab\bar{a}]\cos 3\bar{\sigma}t$$
$$+[b(n_1(b^2-3\bar{b}^2)+n_2(\bar{a}^2-a^2)) - 2n_2 a\bar{a}\bar{b}]\sin 3\bar{\sigma}t\big\}/(9-\bar{\sigma}_{0,1}^2) + o(\epsilon), \tag{A 3}$$

where $n_1 = \frac{1}{2}d_2 + h_0(\frac{3}{2}d_1+2d_3)$, $n_2 = \frac{1}{4}(d_6+d_8+d_{10}+d_{11}) + h_1(\frac{1}{2}d_7+2d_9+d_{12})$, $N_1 = -\frac{3}{4}q_2 + \frac{1}{4}q_4 + h_0(-\frac{1}{2}q_1 - 2q_3 + q_5) - q_1 p_0$, and $N_2 = \frac{1}{4}q_2 + \frac{1}{4}q_4 + h_0(\frac{1}{2}q_1 + 2q_3 + q_5)$.

In similar way, one can get

$$a_3 = \left\{N_1(a^2+\bar{a}^2)[a\cos\bar{\sigma}t+\bar{a}\sin\bar{\sigma}t] - P_{3,0}\eta_{1a}\cos\bar{\sigma}t\right\}/(1-\bar{\sigma}_{3,0}^2) + N_2\left\{a(-a^2+3\bar{a}^2)\cos 3\sigma t + \bar{a}(\bar{a}^2-3a^2)\sin 3\sigma t\right\}/(9-\bar{\sigma}_{3,0}^2)+o(\epsilon), \quad (A\,4)$$

$$c_{21} = \left\{(N_3\bar{a}^2\bar{b}+(N_4-N_3)ab\bar{a}+N_4a^2\bar{b})\cos\bar{\sigma}t + (N_3a^2b+(N_4-N_3)a\bar{b}\bar{a} + N_4\bar{a}^2b)\sin\bar{\sigma}t\right\}/(1-\bar{\sigma}_{2,1}^2) + N_5\left\{(\bar{a}^2\bar{b}+2ab\bar{a}-a^2\bar{b})\cos 3\bar{\sigma}t + (b\bar{a}^2-2a\bar{a}\bar{b}-a^2b)\sin 3\bar{\sigma}t\right\}/(9-\bar{\sigma}_{2,1}^2)+o(\epsilon), \quad (A\,5)$$

$$c_{12} = \left\{(N_3ab^2+(N_4-N_3)b\bar{a}\bar{b}+N_4a\bar{b}^2)\cos\bar{\sigma}t + (N_3\bar{b}^2\bar{a}+(N_4-N_3)b\bar{b}a + N_4b^2\bar{a})\sin\bar{\sigma}t\right\}/(1-\bar{\sigma}_{1,2}^2) + N_5\left\{(ab^2+2\bar{a}b\bar{b}-a\bar{b}^2)\cos 3\bar{\sigma}t + (\bar{a}b^2-2ab\bar{b}-\bar{a}\bar{b}^2)\sin 3\bar{\sigma}t\right\}/(9-\bar{\sigma}_{1,2}^2)+o(\epsilon), \quad (A\,6)$$

$$b_3 = \left\{N_1(\bar{b}^2+b^2)[\bar{b}\cos\bar{\sigma}t+b\sin\bar{\sigma}t] - P_{0,3}\eta_{2a}\cos\bar{\sigma}t\right\}/(1-\bar{\sigma}_{0,3}^2) + N_2\left\{\bar{b}(-\bar{b}^2+3b^2)\cos 3\bar{\sigma}t + b(b^2-3\bar{b}^2)\sin 3\bar{\sigma}t\right\}/(9-\bar{\sigma}_{0,3}^2)+o(\epsilon) \quad (A\,7)$$

from (2.6). Here, $N_3 = -\frac{1}{4}q_7-\frac{1}{4}q_9+\frac{3}{4}q_{12}-\frac{1}{4}q_{13}+h_0(\frac{1}{2}q_8+2q_{10}-q_{15})-q_8p_0+h_1(-\frac{1}{2}q_6-2q_{11}+q_{14})$, $N_4 = -\frac{3}{4}q_7-\frac{3}{4}q_9+\frac{1}{4}q_{12}+\frac{1}{4}q_{13}+h_0(-\frac{1}{2}q_8-2q_{10}+q_{15})-q_8p_0+h_1(-\frac{1}{2}q_6-2q_{11}+q_{14})-q_6p_1$, $N_5 = \frac{1}{4}q_7+\frac{1}{4}q_9+\frac{1}{4}q_{12}+\frac{1}{4}q_{13}+h_0(\frac{1}{2}q_8+2q_{10}+q_{15})+h_1(\frac{1}{2}q_6+2q_{11}+q_{14})$.

Appendix B. Theoretical steady-state wave elevations at the walls

Experiments by Ikeda *et al.* (2012) and Faltinsen *et al.* (2003) deal with measurements of the maximum steady-state wave elevations at the perpendicular walls. The measurements were done slightly away from the walls. For brevity, we can associate the positions of the measured probes with the coordinates $\zeta_x : (\frac{1}{2}Lx_0, 0)$ and $\zeta_y : (0, \frac{1}{2}Ly_0)$.

Neglecting the linearly involved generalised coordinates and using the notations

$$-x_1 = f_1^{(1)}(x_0),\ -y_1 = f_1^{(2)}(y_0),\ x_2 = f_2^{(1)}(x_0),\ y_2 = f_2^{(2)}(x_0),$$
$$-x_3 = f_3^{(1)}(x_0),\ -y_3 = f_3^{(2)}(y_0)$$

computes the wave elevations at ζ_x and ζ_y as

$$\zeta_x(t) = -x_1a_1(t) + x_2a_2(t) - b_2(t) - x_3a_3(t) + x_1c_{12}(t), \quad (B\,1a)$$

$$\zeta_y(t) = -y_1b_1(t) - a_2(t) + y_2b_2(t) - y_3b_3(t) + y_1c_{21}(t), \quad (B\,1b)$$

where the nonlinearly-governed generalised coordinates are accounted for. Substituting the steady-state solution from Appendix A into (B 1) derives the following expressions to approximate the steady-state wave elevations:

$$\begin{aligned}\zeta_x(t) = p_0\left[x_2(a^2+\bar{a}^2)-(b^2+\bar{b}^2)\right] &+ \boxed{\cos\bar{\sigma}t}\left[-x_1a - x_3\left(N_1a(a^2+\bar{a}^2)-P_{3,0}\eta_{1a}\right)/(1-\bar{\sigma}_{3,0}^2)\right.\\ &\left. + x_1(N_3ab^2+(N_4-N_3)b\bar{a}\bar{b}+N_4a\bar{b}^2)/(1-\bar{\sigma}_{1,2}^2)\right]\\ &+ \boxed{\sin\bar{\sigma}t}\left[-x_1\bar{a} - x_3N_1\bar{a}(a^2+\bar{a}^2)/(1-\bar{\sigma}_{3,0}^2)\right.\\ &\left. + x_1(N_3\bar{b}^2\bar{a}+(N_4-N_3)b\bar{b}a+N_4b^2\bar{a})/(1-\bar{\sigma}_{1,2}^2)\right]\\ &+ \boxed{\cos 2\bar{\sigma}t}\left[h_0(x_2(a^2-\bar{a}^2)-(\bar{b}^2-b^2))\right] + \boxed{\sin 2\bar{\sigma}t}\left[2h_0(x_2a\bar{a}-\bar{b}b)\right]\end{aligned}$$

$$+\boxed{\cos 3\bar{\sigma}t}\left[-x_1\left(a[n_1(-a^2+3\bar{a}^2)+n_2(b^2-\bar{b}^2)]+2n_2b\bar{a}\bar{b}\right)/(9-\bar{\sigma}_{1,0}^2)\right.$$
$$-x_3N_2a(-a^2+3\bar{a}^2)/(9-\bar{\sigma}_{3,0}^2)+x_1N_5(ab^2+2\bar{a}b\bar{b}-a\bar{b}^2)/(9-\bar{\sigma}_{1,2}^2)\Big]$$
$$+\boxed{\sin 3\bar{\sigma}t}\left[-x_1\left(\bar{a}[n_1(\bar{a}^2-3a^2)+n_2(b^2-\bar{b}^2)]-2n_2ab\bar{b}\right)/(9-\bar{\sigma}_{1,0}^2)\right.$$
$$-x_3N_2\bar{a}(\bar{a}^2-3a^2)/(9-\bar{\sigma}_{3,0}^2)+x_1N_5(\bar{a}b^2-2ab\bar{b}-\bar{a}\bar{b}^2)/(9-\bar{\sigma}_{1,2}^2)\Big]\,; \quad (\mathrm{B}\,2a)$$

$$\zeta_y(t)=p_0\left[-(a^2+\bar{a}^2)+y_2(b^2+\bar{b}^2)\right]$$
$$+\boxed{\cos\bar{\sigma}t}\left[-y_1\bar{b}-y_3\left(N_1\bar{b}(\bar{b}^2+b^2)-P_{0,3}\eta_{2a}\right)/(1-\bar{\sigma}_{0,3}^2)\right.$$
$$+y_1(N_3\bar{a}^2\bar{b}+(N_4-N_3)ab\bar{a}+N_4a^2\bar{b})/(1-\bar{\sigma}_{2,1}^2)\Big]$$
$$+\boxed{\sin\bar{\sigma}t}\left[-y_1b-y_3N_1b(b^2+\bar{b}^2)/(1-\bar{\sigma}_{3,0}^2)\right.$$
$$+y_1(N_3a^2b+(N_4-N_3)a\bar{a}\bar{b}+N_4\bar{a}^2b)/(1-\bar{\sigma}_{2,1}^2)\Big]$$
$$+\boxed{\cos 2\bar{\sigma}t}\left[h_0(-(a^2-\bar{a}^2)+y_2(\bar{b}^2-b^2))\right]+\boxed{\sin 2\bar{\sigma}t}\left[2h_0(-a\bar{a}+y_2\bar{b}b)\right]$$
$$+\boxed{\cos 3\bar{\sigma}t}\left[-y_1\left(\bar{b}[n_1(-\bar{b}^2+3b^2)+n_2(\bar{a}^2-a^2)]+2n_2ab\bar{a}\right)/(9-\bar{\sigma}_{0,1}^2)\right.$$
$$-y_3N_2\bar{b}(-\bar{b}^2+3b^2)/(9-\bar{\sigma}_{0,3}^2)+y_1N_5(\bar{a}^2\bar{b}+2ab\bar{a}-a^2\bar{b})/(9-\bar{\sigma}_{2,1}^2)\Big]$$
$$+\boxed{\sin 3\bar{\sigma}t}\left[-y_1\left(b[n_1(b^2-3\bar{b}^2)+n_2(\bar{a}^2-a^2)]-2n_2a\bar{a}\bar{b}\right)/(9-\bar{\sigma}_{0,1}^2)\right.$$
$$-y_3N_2b(b^2-3\bar{b}^2)/(9-\bar{\sigma}_{0,3}^2)+y_1N_5(b\bar{a}^2-2a\bar{a}\bar{b}-a^2b)/(9-\bar{\sigma}_{2,1}^2)\Big]\,. \quad (\mathrm{B}\,2b)$$

The maximum theoretical wave elevations at the two measured probes are, therefore, associated with the maximum of the truncated series on the interval $[0, 2\pi]$.

REFERENCES

Ducci, A. & Weheliye, W. H. 2014 Orbitally shaken bioreactors-viscosity effects on flow characteristics. *AIChE Journal* **60** (11), 3951–3968.

Faltinsen, O. M., Rognebakke, O. F. & Timokha, A. N. 2003 Resonant three-dimensional nonlinear sloshing in a square base basin. *Journal of Fluid Mechanics* **487**, 1–42.

Faltinsen, O. M., Rognebakke, O. F. & Timokha, A. N. 2005*a* Classification of three-dimensional nonlinear sloshing in a square-base tank with finite depth. *Journal of Fluids and Structures* **20** (1), 81–103.

Faltinsen, O. M., Rognebakke, O. F. & Timokha, A. N. 2005*b* Resonant three-dimensional nonlinear sloshing in a square base basin. Part 2. Effect of higher modes. *Journal of Fluid Mechanics* **523**, 199–218.

Faltinsen, O. M., Rognebakke, O. F. & Timokha, A. N. 2006*a* Resonant three-dimensional nonlinear sloshing in a square base basin. Part 3. Base ratio perturbation. *Journal of Fluid Mechanics* **551**, 93–116.

Faltinsen, O. M., Rognebakke, O. F. & Timokha, A. N. 2006*b* Transient and steady-state amplitudes of resonant three-dimensional sloshing in a square base tank with a finite fluid depth. *Physics of Fluids* **18** (Art. No. 012103).

Faltinsen, O. M. & Timokha, A. N. 2009 *Sloshing*. Cambridge: Cambridge University Press.

Grundelius, M. 2001 Methods for control of liquid slosh. PhD Thesis, Department of Automatic Control, Lund Institute of Technology, Box 118 SE22100 LUND, Sweden.

Henderson, D.M. & Miles, J.W. 1994 Surface-wave damping in a circular cylinder with a fixed contact line. *Journal of Fluid Mechanics* **275**, 285–299.

Ikeda, T., Harata, Y. & Osasa, T. 2016 Internal resonance of nonlinear sloshing in rectangular liquid tanks subjected to obliquely horizontal excitation. *Journal of Sound and Vibration* **361**, 210–225.

Ikeda, T., Ibrahim, R. A., Harata, Y. & Kuriyama, T. 2012 Nonlinear liquid sloshing in a square tank subjected to obliquely horizontal excitation. *Journal of Fluid Mechanics* **700**, 304–328.

Keulegan, G. 1959 Energy dissipation in standing waves in rectangular basins. *Journal of Fluid Mechanics* **6** (1), 33–50.

Pilipchuk, V.N. 2013 Nonlinear interactions and energy exchange between liquid sloshing modes. *Physica D* **263**, 21–40.

Royon-Lebeaud, A., Hopfinger, E.J. & Cartellier, A. 2007 Liquid sloshing and wave breaking in circular and square-base cylindrical containers. *Journal of Fluid Mechanics* **577**, 467–494.

Shukhmurzaev, Yu.D. 1997 Moving contact lines in liquid/liquid/solid systems. *Journal of Fluid Mechanics* **334**, 211–249.

Wu, Chih-Hua & Chen, Bang-Fuh 2009 Sloshing waves and resonance modes of fluid in a 3D tank by a time-independent finite difference method. *Ocean Engineering* **36**, 500–510.

Wu, Chih-Hua, Chen, Bang-Fuh & Hung, Tin-Kan 2013*a* Hydrodynamic forces induced by transient sloshing in a 3D rectangular tank due to oblique horizontal excitation. *Computers and Mathematics with Applications* **65**, 1163–1186.

Wu, Chih-Hua, Faltinsen, O.M. & Chen, Bang-Fuh 2013*b* Analysis on shift of nature modes of liquid sloshing in a 3D tank subjected to oblique horizontal ground motions with damping devices. *Advances in Mechanical Engineering* **Article ID 627124**, 1–24.

Zhang, Hong-Shang, Wu, Peng-Fei & Liu, Wen-Bai 2014 The analysis of second-order sloshing resonance in a 3-D tank. *Journal of Hydrodynamics* **26** (2), 309–315.